The HadCM3 contribution to PlioMIP Phase 2 Part 1: Core and Tier 1 experiments.

Stephen J. Hunter[1], Alan M Haywood[1], Aisling M. Dolan[1], and Julia C. Tindall[1]

[1]University of Leeds, Leeds, LS2 9JT, UK

Correspondence to: Stephen J. Hunter (S.Hunter@leeds.ac.uk)

Abstract. We present the UK's input into the Pliocene Model Intercomparison Project Phase 2 (PlioMIP2) using the HadCM3 climate model. We outline the process of setting up HadCM3 with the enhanced PRISM4 boundary conditions and discuss in detail the assumptions and choices made. We then present the HadCM3 spin-up process from an initial arbitrary atmosphere, zero-momentum ocean state through to a well-equilibriated climatic state. We present data from the spin-up and final clima-
tological mean state of the pre-industrial and Pliocene experiments. We focus on large-scale climatic and oceanic features. Comparing the control Pliocene experiment to pre-industrial the change in palaeogeography and CO_2 combined account for a warming in globally integrated air temperature (sea surface temperature) of 1.4 ºC (0.8 ºC) and 1.5 ºC (1.0 ºC). For the pre-industrial and Pliocene we see climate sensitivities (for 2 x CO_2) of 3.5 º C and 2.9 ºC. We derive an approximation of Earth System Sensitivity of ∼5.5 º C leading to an ESS/CS ratio ∼ 1.90. Precipitation change is more complex, with geographic
and land surface changes primarily modifying the geographical extent, and increasing CO_2 leading to a general wet-get-wetter response. We see a reduction in summer and winter sea ice extent driven by both geographical - land surface changes and CO_2 increase. In our model, the Atlantic Meridional overturning is relatively insensitive to CO_2 but is strengthened in the Pliocene (from 15.7 to 19.6 Sv) due to the change in palaeogeography. Understanding the change in Antarctic Circumglobal Current within the Pliocene is problematic given an overly intense modern ACC and palaeogeography-driven changes in barotropic
model set-up within the Pliocene. We confirm that the modern orbit used throughout PlioMIP2, is a satisfactory substitute for the Pliocene 3.205 Myr KM5c orbit in terms of large-scale climate and a number of important climatic indices. We also quantify the impact of the total solar irradiance choice (1361 versus 1365 W m^{-2}) on the Pliocene - pre-industrial anomaly and absolute climatic state and highlight climatic systems which may present non-linear responses.

1 Introduction

The Pliocene Model Intercomparison Project Phase 2 (hereafter PlioMIP2 ; Haywood et al. (2016)) has dual focus; to serve as a means to improve understanding of Pliocene climate and also, through its uses a potential analogue for contemporary climate, as a means to evaluate climate model uncertainty. These are referred to as Pliocene4Pliocene (P4P) and Pliocene4Future (P4F). The overall PlioMIP2 experiment design is split up into three components - Core, Tier 1 and Tier 2 experiments. The former are completed by all model groups whilst the optional Tier 1 (T1) experiments are higher priority than Tier 2 (T2). The PlioMIP2 protocol specifies a standard and enhanced boundary condition dataset, the former has a Pliocene topography constrained by

the modern land sea mask and bathymetry whilst the latter has full PRISM4 palaeogeography (Dowsett et al., 2016). Here we describe the model set-up of the enhanced boundary conditions within HadCM3. Table 1 details the PlioMIP2 experiments conducted within this study, which include a set of non-PlioMIP2 experiments that explore additional sensitivities. We conduct all core and Tier 1 experiments as well as the Pliocene4Future Tier 2 experiments. An additional paper will describe the

5 Pliocene4Pliocene Tier 2 (Forcing Factorisation) experiments, and for full consistency with PlioMIP1 (Haywood et al., 2011), a second accompanying paper will describe the set-up and results from the standard boundary condition model experiments.

The structure of this paper is as follows. We first describe the model configuration and then the experiment design (Sections 2 and 3). The generation of model boundary conditions is then detailed (Section 3.2.1) with a focus on efforts to maintain consistency with previous work using HadCM3. This leads onto the model initialisation and spin-up (Section 3.3) and the

10 quantification of the equilibrium state (Section 3.4). The climatological mean state of the experiments is then described within the results, starting with the Atmospheric and surface climatology (Section 4.1) and then the oceanic realm (Section 4.2).

2 Model Description

We use the UK Meteorological Office (UKMO) HadCM3 coupled Atmosphere-Ocean GCM which was used for the first Pliocene model Intercomparison (PlioMIP1). This model was used by the UKMO extensively within CMIP3 (the Third Cli-

15 mate Model Intercomparison Project; contributing to IPCC AR4 Solomon et al. (2007)) but used only for historical and decadal experiments within CMIP5 (IPCC AR5; Flato et al. (2013)), being superseded by HadGEM1 and then HadGEM2-ES respectively. It is no longer state-of-the-art but the models runtime speed, relative ease of reconfiguration, and prediction performance compared to similar generation models make it well suited to long-integration palaeoclimate studies involving the investigation of multiple forcings. HadCM3 can be integrated for many thousands of model years and reaches a satisfactory

20 state of equilibrium with little drift in the surface climatology. However, there are a number of model weaknesses, compared to more contemporary models, these will be discussed where relevant.

The HadCM3 model has been used extensively for studies of the Pliocene, the model was used within PlioMIP1 experiments 1 (Atmosphere GCM) and 2 (Atmosphere-Ocean GCM; Bragg et al. (2012)), and amongst others has been used to successfully investigate Panama seaway closure (Lunt et al., 2008), ENSO and teleconnections (Bonham et al., 2009), ice-sheet recon-

25 structions and orbital forcing (Dolan et al., 2011; Prescott et al., 2014), Terrestrial and marine oxygen isotopes (Tindall and Haywood, 2015), and non-analogous aspects of Pliocene climate (Hill, 2015). In all cases, either a modern land sea mask and bathymetry was used or regional geographical sensitivities were explored. This body of work therefore represents the first published record of HadCM3 has been reconfigured with a bespoke global Pliocene palaeogeography.

A top-level description of the Atmosphere and Ocean models relevant to this palaeogeographic reconfiguration follows. A

30 focus is given to the ocean model as its external geometry is changed (the atmosphere model layers drapes over the topography) and certain aspects impact upon the interpretation of model prediction. For a more comprehensive description of the fundamental model structure see Pope et al. (2000) and Gordon et al. (2000). Valdes et al. (2017) describes corrections and improvements that have been made since 2000 as well as a thorough evaluation against observational data. The HadCM3 model used in this

study is equivalent, in terms of model updates and modifications, to HadCM3B-M2.1a of Valdes et al. (2017). We keep with the name HadCM3 in reference to the UKMO (Pope et al., 2000; Gordon et al., 2000) but acknowledge the contribution made by the University of Bristol in keeping the HadCM3 developed and updated.

2.1 Atmosphere model

5   The atmosphere component of HadCM3 has 19 vertical hybrid sigma-pressure levels (5 terrain-following sigma-levels at the surface changing to pressure-levels at height, extending to 10 hPa). Horizontal resolution is 3.75 x 2.5° (96 longitude x 73 latitude), equivalent to 417 x 278 km and 295 x 278 km at the equator and 45° latitude respectively. The model has a time-step of 30 minutes and is coupled to the ocean model (Section 2.2) using the oasis coupler every model day. Atmospheric composition, other than CO_2 (described in Section 3.1 and 3.2) is equivalent to pre-industrial throughout (N_2O 270 ppb, CH_4 760 ppb and

10 no CFC) consistent with the PMIP2 protocol (Braconnot et al., 2007). We chose PMIP2 so as to remain consistent with the previous Pliocene experiments conducted within PlioMIP1. Monthly distribution of ozone is derived from the Li and Shine (1995) climatology and ground-based troposphere measurements, corrected for the ozone hole (Hadley Centre technical Note 22; Johns et al 2001). The radiative effects of background aerosol are represented by a simple parameterisation based upon the modern (Cusack et al., 1998).

15 The solar constant (total solar irradiance; hereafter TSI) is held fixed at 1365.0 Wm⁻² within *all* experiments, a value consistent with the pre-industrial experiment within PMIP2 and CMIP5 as well as PlioMIP1. We use this often used canonical value (derived in the 1990s) to remain consistent with previous work but acknowledge that space borne measurements of TSI have decreased from 1,371 to 1362 Wm⁻² from 1978 to 2013 (Kopp and Lean, 2011; Meftah et al., 2014). Indeed, the CMIP6 *piControl* simulation uses a value of 1361 Wm⁻² (Matthews et al., 2016). We examined the impact of TSI choice within the

20 context of both pre-industrial and Pliocene climates (Section 4.3.2). Recognising this source of uncertainty and the impact on climate anomalies (due to non-linear climate responses) is important as the PlioMIP2 specification (Haywood et al., 2016, Section 2.3.1) leaves the choice of TSI to individual modelling groups, whose TSI may depend upon if the group is participating within CMIP6. The impact of TSI choice is minimised by the Pliocene communities use of climatological anomalies, but should be considered when comparing model-model absolute indices (summer sea ice extent, AMOC strength etc.).

25 The land surface scheme is MOSES 2.1 (Met Office Surface Exchange Scheme; Cox et al. (1999). Within the scheme there are 5 plant functional types (PFTs: Broadleaf and Needleleaf trees, C_3 and C_4 grasses, and shrub) as well as soil (desert), lakes and ice. Each terrestrial grid cell can take fractional values of each surface type, except if it is glaciated, which is unitary. We hold vegetation fixed through the entirety of each experiment. MOSES principally deals with the hydrology of the canopy to the subsurface, and the surface energy balance (including subsurface thermodynamics). MOSES2 introduced subgrid (tiled)

30 heterogeneity and improved representation of surface and plant processes.

Runoff is collected in drainage basins and delivered to associated coastal outflow points (on a 3.75 x 2.5° geographic grid). River transport is not modelled explicitly, instead runoff is returned to the coastal outflow point in the upper layer of ocean instantaneously (at the atmosphere-ocean coupling step).

2.2 Ocean Model

The ocean component is a rigid lid model of the Bryan-Cox-Semtner lineage (Bryan, 1969; Semtner, 1974; Cox, 1984). In the vertical there are 20 unevenly-spaced levels, concentrated near the surface (8 in the top 200 m) in an attempt to improve representation of the surface mixed layer. The ocean time-step is 1 hour. The model uses z-type cells with bottom topography represented by "full" cells. Horizontal spatial resolution is 1.25º (288 x 144 geographic grid) giving 6 grid cells per atmospheric model cell. The land-sea mask is effectively 3.75 x 2.5º resolution in the top 200 m but beneath increases to 1.25º lateral resolution.

Within the modern boundary conditions, cells overlying important subgrid-scale channels are artificially deepened to improve flow representation (Denmark Strait, Iceland-Faroe and Faroe-Shetland Channels, and the Indonesian archipelago). Additionally, within the Greenland-Iceland-Scotland region a convective adjustment scheme (Roether et al., 1994) is used to better represent down-slope mixing; important for the representation of dense outflows that form the North Atlantic Deep Water (NADW). A similar scheme is not present for Antarctic Bottom Water. Water mass exchange through the Strait of Gibraltar, a channel that falls sub grid-scale, is achieved with a diffusive pipe. Other sub grid-scale channels, such as the Canadian Archipelago, Hudson Bay outflow and the Makassar Strait, remain spatially unresolved and subsequently unrepresented. The latter has been shown to possess most of the Indonesian throughflow (Gordon et al., 2000) and so is compensated for within the model by a deepening of regional model bathymetry. The fresh water budget of the ocean is balanced by fresh water fluxes (specifically, virtual -ve salinity fluxes) from the river routing scheme and a prescribed time-invariant freshwater iceberg field. Within the Pliocene experiments we omit the latter and instead use an annually derived freshwater correction to reduce residual globally-integrated salinity drifts to zero, and hence artificiality close the water budget. We justify this as we currently do not have *a priori* knowledge of the geographic distribution of iceberg melt consistent with the ice sheet distribution within the PlioMIP2 enhanced boundary conditions. In the northern hemisphere we do not expect significant iceberg calving given the configuration of the Greenland ice sheet and the lack of marine terminating margins specified within the PRISM4 boundary conditions.

The rigid lid streamfunction scheme imposes the need for bathymetry to be smoothed particularly in steep regions of the high-latitudes, and for islands to be specified as line integrals for the barotropic stream function. A major consequence of the latter is that the modern Bering Strait through-flow is not fully resolved as it sits between two model-defined continents between which the barotropic component of flow is poorly resolved. An advantage of the rigid lid scheme is that barotropic gravity waves are neglected which facilitates the use of longer time-steps.

The sea ice model is a simple thermodynamic scheme with parameterisations for ice drift and concentration (including leads). Observation derived upper-boundaries to Arctic and Antarctic sea ice concentration of 0.995 and 0.980 are used. Ocean salinity is influenced by sea ice formation and melt by assuming a sea ice salinity of 0.6 psu (excess salt, in effect, is returned to the ocean). Sublimation is represented and acts to increase ocean salinity (salt blown into leads), whilst ocean-bound snowfall and precipitation reduce salinity. The effects of snow age and melt pond formation on surface albedo is represented with a simple parametersisation. Ice drifts only by the action surface ocean current. Sea ice dynamics is represented by parameterisation

based upon Bryan (1969) and ice rheology is simply represented by preventing ice convergence above 4 m thickness. There is no representation for the interaction between floes.

3 Experiment Design

We now describe the setup of the Pliocene and pre-industrial experiment. The Pliocene experiments have CO_2 set to 280, 350, 400, and 450 ppmv, each conducted with modern orbit as specified by the PlioMIP2 protocol, and a 3.205 Myr orbit consistent with the KM5c time slice. The modern-orbit Pliocene experiments are labelled Eoi^{400} (PlioMIP2 Core experiment), $Eoi^{350,450}$ (Tier 1; P4F+P4P), and Eoi^{280} (Tier 2;P4F). Here we use a comma separated list in the superscript to indicate 2 or more experiments. In all cases, the superscript indicates CO_2 (in ppmv) and the o and i indicate PRISM4 orography and ice-sheet, the former includes PRISM4 vegetation, soil, and lakes. The pre-industrial experiments are run at 280, 400, and 560 ppmv, giving E^{280} (Core), E^{400} (Tier 2; P4F) and E^{560} (Tier 1;P4F) components of PlioMIP2 experiment design. We use a preceding subscript to indicate a sensitivity outside the PlioMIP2 protocol. We explore two sets of non-protocol sensitivities - orbit and solar insolation. The 3.205 Myr orbit experiments (the standard is modern orbit) are distinguished by *orb*, such as $_{orb}Eoi^{400}$, and total solar irradiance (Section 2.1), are labelled $_{1361}E^{280}$ and $_{1361}Eoi^{400}$.

For convenience when referring to climate forcing, we use the term *palaeogeography* to encompass the combined change in topography, land surface (vegetation, lakes, soils, ice sheets), land sea mask and bathymetry (Eoi^{280} - E^{280}).

3.1 Pre-industrial experiment description ($E^{280,400,560}$ and $_{1361}E^{280}$)

The pre-industrial experiments are 500 year continuations of a long integration (>2500 model year) pre-industrial experiment that had been initialised from Levitus observed ocean state (Levitus and Boyer 1994). The experiment uses a topography and a bathymetry regridded and smoothed from ETOPO5 (Edwards 1989), and vegetation and soil translated from Wilson and Henderson-Sellers (1985) land cover. River routing is derived by aggregating runoff in all terrestrial grid boxes within each basin in a manner which is internally consistent with the model topography. All model boundary conditions were developed by the Met Office Hadley Centre (hereafter MOHC) and used within CMIP3/5. In accordance to the PlioMIP2 protocol, levels of atmospheric CO_2 is 280, 400 and 560 ppmv. A fourth pre-industrial experiment, $_{1361}E^{280}$, is run to allow derivation of the model sensitivity to the choice in total solar irradiance (Section 2.1 and 4.3.2).

3.2 Pliocene (PlioMIP2 enhanced) experiment description ($Eoi^{280-450}$, $_{orb}Eoi^{280-450}$, and $_{1361}Eoi^{400}$)

3.2.1 Boundary condition preparation

PlioMIP2 enhanced and modern boundary conditions are provided on regular 1° grids held within NetCDF files. For convenience we shall refer to the PlioMIP2 enhanced boundary condition as PRISM4. The modern boundary condition is provided to facilitate the anomaly method of boundary condition generation. The land sea mask is first regridded by computing the anomaly of PRISM4 pliocene minus modern (at 1° resolution), regridding using bilinear interpolating from 360 x 180 to the 96 x 73

model grid, and then applying the anomaly to the models pre-industrial land sea mask. This is so that the final reconstruction is consistent with both the original MOHC model set up (regridding methodology and hand edits) and the PRISM4 land sea mask (LSM). Furthermore, a number of hand edits were then applied to the resulting 96 x 73 PRISM4 LSM to ensure that the underlying character of the PRISM4 reconstruction is represented as best as reasonably practicable at model resolution. In par-

5 ticular hand edits were applied in the Eurasian Arctic, Baffin Bay, Greenland, North America, Europe and the Mediterranean, Africa, South America, Australasia and Antarctica. In remaining consistent with the MOHC developed pre-industrial boundary conditions we omit Svalbard and Novaya Zemlya despite subaerial extension within PRISM4. At model resolution the Strait of Gibraltar is the same as pre-industrial and so the diffusive pipe is incorporated.

The resulting PRISM4 LSM was then used to constrain the generation of the model resolution orography and bathymetry

10 which were interpolated using similar methodology, and then applied as an anomaly to the existing HadCM3 pre-industrial orography and bathymetry. River routing was derived from the pre-industrial routing scheme (Section 3.1) but corrected in regions of land sea mask, topographical and ice-bedrock change using a model resolution river routing model. This is then followed by manual correction in corrected regions in circumstances when model resolution fails to capture important orography or where new orography is flat. The vegetation scheme was regridded by combining a BIOME4-to-MOSES2 lookup table and

15 bespoke regridding methodology relying on an area-weighted survey of underlying biomes, guided by the model resolution LSM. A similar area-weighted regridding was conducted for the lake field. We chose not to generate the lake mask as an anomaly from the modern lake distribution as land surface change since the pre-industrial would be imprinted on the models lake distribution. All boundary conditions were generated within a bespoke Matlab framework using the MOHC-developed and National Centre for Atmospheric Sciences, Computing Modelling Services (NCAS-CMS) supported xancil and um2nc

20 tools.

3.2.2 Barotropic streamfunction Island configuration

Rigid lid Bryan-Cox type models require islands (and by extension, continents) to be identified so that a net non-zero barotropic flow (depth-independent) can be achieved around the line integral (streamfunction non-zero). The default pre-industrial configuration of the model has 6 islands defined. For consistency, aforementioned hand edits to both land sea mask and bathymetry

25 have allowed islands to be specified that are consistent with the E^{280} experiment but also reflect the key palaeogeographic changes presented by the PRISM4 palaeogeography. In particular western Iceland and East Greenland land cells were adjusted to ensure that Iceland could be defined as a streamfunction island, and hence we could represent fully the East Greenland Current. The island to the west of the Antarctic Peninsula body, lies within the island definition of the main Antarctic continent and therefore the circulation between the two is not fully resolved (only the Baroclinic flow is resolved fully). Figure 1 compares

30 the pre-industrial and PRISM4 HadCM3 island specification. Within PRISM4, 8 islands have been specified.

It is noted that within pre-industrial HadCM3 experiment the Bering Strait barotropic component of throughflow is poorly resolved and both the Makassar Strait and the Canadian Archipelago are spatially unresolved (Section 1.1). This poses a conceptual problem in the interpretation of the Pliocene experiments with respect to the pre-industrial, as the PRISM4 boundary conditions specifies these throughflow regions as closed. Therefore, we will not see the full climatic response of regional

palaeogeographic changes, when we look at climatological anomalies. A pre-industrial experiment with a resolved Bering Strait and Canadian Archipelago would partially resolve these problems but would then force a divergence away from the previous HadCM3 descriptions and evaluations, as well as past and current CMIP/PMIP and PlioMIP model implementations. These problems are likely to arise in all rigid rid streamfunction ocean models that have insufficient spatial resolution to fully-

5 resolve these channels and inherently cannot resolve line integrals around bounding land masses. Ocean models that have explicit or implicit free surface schemes with sufficiently high horizontal spatial resolution may resolve these issues.

3.3 Pliocene Model initialization and spin up

Model spin-up is conducted in eight stages. First the Atmosphere model (AGCM) was initialized in a 50 year run with PRISM4 basic surface scheme (lakes, ice, shrubs and orography) and land sea mask, pre-industrial CO_2 and zonal hemispheric-

10 symmetric monthly Sea Surface Temperature (SST) and sea ice derived from a well spun-up pre-industrial HadCM3 (AOGCM) simulation. Model failures at this stage allow for the identification of steep topography that requires regional smoothing. This is then followed by a 100 year AOGCM run with PRISM4 bathymetry and the river scheme. Here the ocean model has barotropic physics turned off. Stage three adds the barotropic physics (without specifying islands) and runs for 200 years. Regional bathy-metric smoothing was applied in regions which caused model failure. The island configuration (Section 3.2.2, Figure 1) is then

15 derived in stage four using an iterative series of sensitivity tests in which each island configuration is refined. Once complete, the set of island line integrals are then incorporated into the model configuration (1. At stage five we have an AOGCM incorpo-rating full barotropic physics, CO_2 is then ramped up at 1% per year to 400 ppm and then held fixed. At model year 950, stage six, a problem with ancilliary file generation had been resolved allowing the vegetation boundary conditions to be incorporated into the model. Additionally, a regional modification was made to the bathymetry and streamfunction island configuration to

20 the west of the Antarctic Peninsula following a persistent and unsatisfactory model artefact in this region. The model was then set to continue (CO_2 held fixed at 400 ppmv). At year 2000 we reached stage seven at which 3 further experiments at 280, 350 and 450 ppmv are spun-off (as well as the four KM5c 3.205 Mya orbit experiments). All 8 experiments are run to year 2400. At the final stage, stage eight, the models are run for the final 100 years with full climatological output. The final 50 years is used for climatological averages.

25 In total the ten Pliocene experiments (Core and Tier 1 detailed within Table 1 as well as $_{orb}Eoi^{400}$, $_{1361}E^{280}$, and $_{1361}Eoi^{400}$) were run for 7000 model years giving a total of 7.5Tb of data. Each instance of the model is run on 24 Intel Xeon E5-2650v4 cores of the University of Leeds Advanced Research Computing platform (ARC2) and with full physics achieve 70-90 model years per wall clock day depending upon the chosen diagnostic output suite.

3.4 Equilibrium State

30 By model years 2400 to 2500, our Pliocene control experiment Eoi^{400} has achieved a quasi-steady-state equilibrium in which the globally-integrated net top-of-the-atmosphere (TOA) radiative imbalance is +0.047 W m^{-2}, surface (1.5 m) air temperature trend is +0.08 ^{0}C century^{-1} and the upper 200 m and globally integrated ocean potential temperature trends are -0.026 ^{0}C century $^{-1}$ and +0.041 ^{0}C century^{-1} respectively. The corresponding values for the pre-industrial control, E^{280} are -0.115 W

m^{-2}, 0.052 ^{o}C century^{-1} ,and -0.014 ^{o}C century $^{-1}$ respectively. High CO_2 experiments, Eoi^{450} and E^{560} present the largest, yet modest, disequilibrium represented by TOA imbalance > 0.2 Wm^{-2}. Positive TOA imbalance is indicative of a warming, the small heat capacity of the atmosphere and land means that residual energy is taken up by the ocean, which is reflected in the volume averaged ocean temperature evolution.Warming of the deep ocean is primarily occurring at depths of >2000

5 m of the Pacific basin. The Indian and Antarctic oceans are the most equilibriated of the oceans particularly at intermediate depths and greater. Table 2 summarizes the equilibrium state of the seven PlioMIP2 experiments and Figure 2 presents the time-evolution of ocean temperature. All experiments are satisfactory, although E^{560} has above average warming within the deep ocean. Derivation of climatological trends within the surface climatology of the last 100 model years is inconsistent as the trend is small compared to the climatological standard deviation.

10 ## 4   Results

We derive climatological averages from the final 50 yrs (model years 2450-2499) and climatic oscillations from the final 100 years. We principally compare the two core experiments (Eoi^{400} and E^{280}).

4.1   Atmospheric and surface climatology

4.1.1   Surface Air Temperature and Climate Sensitivity

15 Modelled mean annual temperatures (hereafter MAT) are detailed within Tables 3 and Figure 3. Relative to the pre-industrial control (E^{280}) temperatures are generally warmer within the Pliocene experiments. Differences in MAT of up to 31.3 ^{o}C coincide with Greenland and Antarctic regions of Pliocene ice sheet retreat (and topographical reduction). Typically, warming is greatest over land although in ocean regions at or near Antarctic land sea mask change (terrestrial ice to Pliocene ocean) warming is significant. This pattern of warming is in a similar distribution to HadCM3 within PlioMIP under PRISM3 boundary

20 conditions (Bragg et al., 2012, Exp. 2).

The Pliocene cooling in the Barents sea is statistically significant and persistent through the model integration. It coincides with an increase in Pliocene winter and spring sea ice concentration driven by palaeogeographic terrestrial winter cooling in the circum-Arctic (Pliocene subaerial Barents and Baltic Sea). This cooling is potentially driven by the partial suppression of northward heat transport (in the Norwegian Current) by the sub-aerial extension of the UK region within the model.

25 Figure 4 shows the Annual and Seasonal temperature anomalies for Eoi^{280} and Eoi^{400}. Terrestrial regions, such as the Hudson Bay and Baltic Sea regions, that are subareal only within the Pliocene (marginal seas in the present) are $> 10^{o}$ C warmer (colder) during he summer (winter) seasons, due to land-ocean heat capacity contrast. It is unclear how much of this seasonal temperature response in the Baltic Sea region (sub-areal during the Pliocene) is a driver of persistent cooling within the Barents Sea region.

From Table 3 it is possible to decompose the factors that contribute to Pliocene warming relative to the pre-industrial E^{280}. The change in palaeogeography and land surface (Eoi^{280}-E^{280}) accounts for a temperature change of 1.4 ± 0.7°C, whilst the increase in CO_2 (Eoi^{400}-Eoi^{280}) accounts for a further 1.5 ± 0.7°C warming.

The Climate Sensitivity to a doubling of CO_2 (CS_{2xCO_2}) for the pre-industrial is 3.5 ± 0.7 ° C, whilst for the Pliocene

5 (derived from Eoi^{400} and Eoi^{280} and scaled by 1.88 (=log(560/280)/log(400/280))) is $2.9 \pm \sim 1.0$ ° C. The pre-industrial CS is consistent with the 3.3° C for HadCM3 within CMIP3 (Randall et al., 2007) and the Pliocene CS_{2xCO_2} is similar to the 3.1 ° C HadCM3 value from PlioMIP1 Experiment 2 (Table 2; Haywood et al., 2013). When we neglect geographical changes and approximate Earth System Sensitivity (ESS) from Eoi^{400} and E^{280} (using 1.88 x $\triangle T_{Eoi^{400} - E^{280}}$) we obtain $\sim 5.5 \pm \sim 1.3$ ° C. Subsequently the ESS/CS ratio is ~ 1.90, which again is similar to the ESS/CS ratio of 2.0 of HadCM3 within PlioMIP1

10 (Haywood et al., 2013). It must be noted that this calculation assumes that the PlioMIP2 enhanced boundary condition *is* the equilibriated Earth System to a contemporary doubling of CO_2, hence neglecting changes in topography and land sea mask.

4.1.2 Precipitation

The globally integrated Mean Annual Precipitation metric (MAP; Table 4), is influenced principally by geography and land surface changes and is relatively insensitive to Pliocene CO_2 changes. The change in palaeogeography (Eoi^{280} - E^{280}) modifies

15 the distribution of precipitation as can be seen within Figure 5. Northern hemisphere land masses generally see increased precipitation although this effect is minimal in the continental interiors. In the southern hemisphere much of South America and South Africa receives less precipitation whilst Australia sees an increase in precipitation. Increasing Pliocene CO_2 generally intensifies the precipitation anomaly which is most apparent in the tropics. Regions that have little (< 0.1 mm day^{-1}) change in precipitation are regions that receive little precipitation within E^{280} - North Africa and the East Antarctic Ice Sheet. Therefore,

20 the models response to elevating CO_2 in the Pliocene context seems to largely follow the wet get wetter paradigm.

Seasonal plots of precipitation change can be seen within Figure 6. During the Pliocene we see wetter summers over much of North America and northern Europe. Regions seeing reduced precipitation in western North America as well as central and western Europe are a consequence of weakened westerlies.

The Pliocene geography and land surface change drive an intensification of precipitation associated with the Inter Tropical

25 Convergence Zone (ITCZ) although changes in seasonal latitudinal distribution is not evident. The south Pacific Convergence Zone, extending from the western Pacific warm pool southeastward to the south central Pacific extends ~ 15° more eastward in E^{280} than Eoi^{400} and Eoi^{280}, Depsite this, a double-ITCZ is not otherwise present as commonly found in other GCMs (Li and Xie 2014), for example within the Western pacific. or extension into the South Atlantic is not present.

To understand changes in monsoon dynamics it is important to assess the underlying model performance. Here we consider

30 the the South American and Indian monsoons. Within E^{280} the seasonal timing and geographic distribution of the South American Monsoon System (SAMS) precipitation cycle is adequately represented although the intense precipitation is too far southward, focussed too zonally at 15° S (cf. 10 - 30° S). Within E^{280} the seasonal shifts in the overlying atmosphere (e.g. the tropospheric anticyclone (250-hPa) and 925-hPa wind field) are well-represented, although the ITCZ precipitation is overly intense. During the dry season (JJA-SON) the general pattern of rainfall and dryness is captured. The change in land surface

(Eoi^{280}-E^{280}) drives an intensification of the SAMS wet season over east and central Brazil as both the ITCZ and South Atlantic Convergence Zone (SACZ) intensify. Outside the SAMS region the austral winter becomes drier. As CO_2 increases a reduction in wet season precipitation in eastern Brazil coincident with increased precipitation to the west is predicted. Pliocene CO_2 has a much smaller ($<$ 1 mm day^{-1}) influence on austral winter precipitation (SAMS dry season).

5   The Indian monsoon is represented fairly well within E^{280}, we see the seasonal switch from dry North Easterlies to wet South Westerlies. With the change in palaeogeography (Eoi^{280}-E^{280}) the mean summer (JJAS) rainfall increases by up to $\sim$200% in the North West and generally 60-160% over the remainder of India. With the increase in Pliocene CO_2 (from Eoi^{280} to Eoi^{400}) we see a slight reduction in precipitation of up to 7%.

4.1.3   Planetary scale atmospheric circulation.

10   The time averaged zonal mean meridional mass stream function for the atmosphere is shown within Figure 7. Clearly distinguished are the Hadley, the indirect Ferrel and the polar cells. The mean meridional circulation is sensitive to equatorial asymmetries in surface temperatures as ascent in the tropical belt and subsidence in the subtropics form the Hadley cells. Assuming the maximum in meridional streamfunction represents Hadley cell strength, we find that the Pliocene geography acts to weaken (intensify) the Hadley cell within the northern (southern) hemisphere. Looking at E^{280} we find the northern cell is

15   stronger (+10.8%) than the southern which is in contrast to observational and re-analysis data (Stachnik and Schumacher 2011) that show consistently the southern cell being stronger than the northern cell. With increasing Pliocene CO_2 the southern cell intensifies and becomes stronger than the north (+19% for Eoi^{280} and +42% for Eoi^{400}). This intensification (weakening) of the Hadley cell under changed land surface and geography should be driven by steepening (shallowing) of the tropical meridional temperature gradients in the Tropics south (north) of the ITCZ. Coincident with the change in land surface and geography

20   (Eoi^{280}-E^{280}) is a weakening of the combined annual mean overturning within the two Hadley cells (191 and 180 x10^9 kg s^{-1} for E^{280} and Eoi^{280} respectively).

The wintertime Subtropical Jet (StJ; also known as the midlatitude jet) and Polar Jet streams (PJ) are shown within Figure 8. We characterise the mean spatial envelope of the jet path by deriving from 50 years of daily data, the days per season in which the mean mass-weighted flow speed integrated over 400 - 100 hPa ($\sim$7 -16 km) exceeds 30 ms^{-1}. For both E^{280} and E^{400}

25   we obtain a seasonal jet stream configuration which is consistent with the ERA-40 and derived results of Archer and Caldeira (2008). The polar jet and the Subtropical jet stream can be difficult to differentiate as the former is latitudinally irregular, so following Koch et al., (2006) we use normalised wind shear as a height differentiator. The Subtropical jet stream path is more persistent and stable latitudinally and so we characterise the mean response of the jets to changing boundary conditions by the mean latitude of the Subtropical jet core, shown within Table 5. The change in geography (Eoi^{280} -E^{280}) drives a poleward shift

30   of the mean jet of $\sim$1.6º in the northern hemisphere (both seasons) and 2.2º in the southern hemisphere summer. The response to Pliocene CO_2 (Eoi^{400} -Eoi^{280}) increase is weaker with a 0.8º poleward shift in the northern hemisphere (both seasons). The summer hemisphere mean jet appears only weakly poleward shifting in response to Pliocene CO_2 increase. Regionally, jet behaviour deviates from the global mean view. Within the North Atlantic, the polar jet moves equaterwards in response to the change in palaeogeography (Eoi^{280} -E^{280}) moving the jet stream mean path from northern to southern Europe. Synoptic storms

grow and propagate along jet stream axis and so this equaterward shift in polar jet likely contributes to the increase in rainfall seen in southern Europe during Pliocene wintertime (Figure 6e).

4.2 Ocean state: Description of the gross hydrographic, circulation features, Overturning and ocean heat transports.

4.2.1 Sea Surface Temperature and Warm Pools

5 Pliocene and preindustrial Mean Annual SST (MASST) are detailed within Table 6 and shown within Figure 9. We see a 0.8^o C warming due to the change in palaeogeography (Eoi^{280} - E^{280}) and a further 1.0^o C of warming due to the change in Pliocene CO_2 (Eoi^{400} - E^{280}). With increasing levels of CO_2 regional patterns of SST change due to palaeogeography are overprinted by CO_2 induced warming. This warming is most evident in the temperate zone (mid latitudes), particularly within the North and South Atlantic and the North Pacific.Within the North Atlantic subpolar gyre where Eoi^{400} - E^{280} reaches $+9.3^o$
10 C. In the vicinity of the modern Gulf Stream and North Atlantic Drift we find a cooling during DJF and MAM seasons (up to -4.9^o C within Eoi^{280} - E^{280}). Investigation of surface ocean vectors (not shown) suggests an intensification of the North Atlantic wind-driven subpolar gyre and Labrador current which appears to disrupt western intensification and the path of the Gulf Stream, although the expression of the Gulf Stream within HadCM3 surface ocean vectors is limited. The westerlies in the region appear to intercept the remnant gulf stream and divert it from a north easterly to a more eastward path, this is seen
15 as the warm tongue south of the extant Gulf stream (Figure 9). A similar expression of SST within the North Atlantic was seen by Chandler et al. (2013) and characteristic signatures may be present within other PlioMIP1 experiments (e.g. Figure 1 of Dowsett et al. (2013)). A persistent cooling is also found within the Barents sea region coincident with the surface air temperature anomalies discussed within Section 4.1.1. Longitudinal filaments of warmth extending eastward from Japan and Argentina are characteristic of the model.

20 Table 6 also details the size of the global and component equatorial warm pools within the preindustrial and Pliocene experiments. We see an expansion of the globally-integrated warm pool with the change in palaeogeography (Eoi^{280} - E^{280}), but this effect diminishes with increased CO_2. This is evident in both the Western Hemisphere Warm Pool (WHWP) and Indo - Pacific Warm Pool (IPWP) regions. As expected, increased CO_2 drives warm pool expansion.

4.2.2 Sea Ice

25 A complex picture emerges in the geographic and CO_2 sensitivity of seasonal sea ice distributions as shown within Figure 10. Within northern hemisphere winters, the paleaogeographic and vegetation changes (Figure 10g vs. 10c) drive an equaterward expansion of sea ice extent in the Greenland Sea region. Increasing CO_2 from 280 to 400 ppm counteracts some of this expansion. In the southern hemisphere the palaeogeographical changes suppresses sea ice extent significantly within the Weddell Sea and also eastward towards the Davis Sea in both summer and winter. Coincident with this suppression, is an equaterward
30 expansion of sea ice within the Bellinghausen Sea region. Generally as we increase CO_2 at both poles we see a general reduction in the sea ice extent and ice concentration in both summer and winter months. Within Eoi^{400} boreal summer the Arctic is largely ice-free, the ice that is present is mostly <50% concentration. During Austral summer the concentration of sea ice

within the Pliocene becomes more asymetric and reduced in extent - being concentrated in the highest latitudes on the coast of West Antarctic.

4.2.3 Mixed Layer Depth and Deep Water Formation

Here we rely upon the mixed layer depth (MLD) as calculated as a diagnostic variable within HadCM3 climate model. Deep
5   convection is a principle mechanism of deep water formation (DWF). E^{280} represents fairly well the modern open-ocean deep convection that occur within localised areas of the Weddell and Ross Seas (these form the main formation sites of Antarctic Bottom Water) and in the Labrador, Irminger and Greenland seas. All Pliocene experiments exhibit much more widespread deep convection particularly within the Labrador and Norwegian Seas, and off of the island Antarctic Peninsula. It should be noted that deep convection is highly localised and model representation is only suggestive. In contrast to Burls et al. (2017) we
10 do not model any significant increase in Pliocene North Pacific MLD, and hence no subsequent intensification of North Pacific Deep Water (NPDW) formation (see Table 7).

4.2.4 Ocean Heat and Mass Transports (Atlantic and Pacific MOC)

The Atlantic Meridional Overturning Circulation (AMOC) streamfunction for E^{280}, Eoi^{280} and Eoi^{400} is shown within Figure 12 and detailed within Table 7. We find consistency between E^{280} and E^{400} and the observed 17.2 ± 4.6 Sv (RAPID array 26.5º
15 N Apr 2004 - Oct 2012 ;McCarthy et al., 2015) [1 Sv = 10^6 m^3]. Our E^{280} $AMOC_{max}$ differs to the 17.6 Sv of Bragg et al., (2012), a difference we ascribe to the latter use of HadCM3 MOSES 1. The time-mean maximum strength within Eoi^{400} is 19.6 Sv and occurs at $\sim$1000 m. depth at 33.75º N. Fluctuations of the order in the AMOC index are visible in the Pliocene experiment but not the pre-industrial (Jackson and Vellinga 2012). In all cases the maximum in AMOC occurs within the 25 - 33.75º N zonal envelope and at a depth of $\sim$ 650 m. Despite an intensification of the AMOC in Pliocene experiments, we find
20 that the overturning strength drops of slightly at $\sim$40 º N driven by the changed land surface and bathymetry (Eoi^{280}-E^{280}). This is seen within cooling evident in Gulf Stream SSTs of Figure 9. Under increasing Pliocene CO_2, the mid-latitude overturning intensifies with a corresponding decrease in the Gulf Stream SST cold anomaly. The overturning within the polar region is evidence of bottom water formation within the Nordic seas. In E^{280} overturning extends to $\sim$80 º N but is weaker than in the Pliocene models (which extend to $\sim$75 º N). This is reflected within the geographic extent and intensity of deep convection
25 shown within Fig 11.

The Pacific Meridional Overturning Circulation (PMOC) is shown within Figure 13 and detailed within Table 7, in which $PMOC_{+ve}$ reflects the strength of the subtropical gyre circulation whilst $PMOC_{-ve}$ reflects the strength (and depth) of the Pacific Deep Water (PDW) and North Pacific Deep Water (NPDW). Palaeogeography (E^{280} - Eoi^{280}) drives an intensification of both the subtropical gyre and PDW overturning whilst increasing Pliocene CO_2 acts to weaken them. Nevertheless the Pliocene
30 subtropical gyre and PDW overturning are stronger regardless of CO_2 level (Eoi^{400} is 22% and 6 % stronger than E^{280}). With the change in palaeogeography (E^{280} - Eoi^{280}) the PDW shoals (from 4 to 3 km) and with increasing Pliocene CO_2 the NPDW overturning reduces in northward reach, this is associated with the warming of North Pacific SSTs of Figure 9.

4.2.5 Antarctic Circumglobal Current

The Antarctic Circumglobal Current (ACC) strength is detailed within Table 8 and shown within Figure 14. We calculate the volumetric flow of the Antarctic Circumpolar Current at the Drake passage across a 64.375 - 56.875º S 65W transect using the positive aspect of the U component (zonal) of the total (Barotropic and Baroclinic) velocity.

5   We find an overly intense ACC within E^{280} and E^{400} when comparing to recent observations of between 134 - 164 Sv (Cunningham et al., 2003; Griesel et al., 2012), this aspect of HadCM3 has been identified previously. Considering CMIP5 historical experiments, Meijers et al. (2012) found that HadCM3 over the period 1976 to 2005 had an ACC at the Drake Passage transect of 244.5 ± 4.0 Sv, which compared unfavourably to aforementioned observations and the CMIP5 multi-model mean of 155 ± 51 Sv. This unrealistic intensity appeared to be driven, or at least connected to, an overly strong salinity gradients

10   across the ACC, particularly on the equaterside. This could be a consequence of the artificial fresh water correction field used within the CMIP5 historical and piControl experiments and the E^{280} here.

Modelled ACC strength appears significantly reduced within the Pliocene experiments. Westerlies intensify within the Pliocene but mostly in regions poleward of the Sub-Antarctic front (poleward of the ACC). The weakened Drake Passage throughflow is mirrored within the vertically integrated barotropic stream function. Care must be taken when interpretting

15   ACC strength in situations of changed palaeogeography and island specification. The ACC is weakly stratified and vertically coherent and so is dominantly barotropic in nature. Within the Pliocene boundary conditions (Section 3.2.2) the island Peninsula is defined as a separate barotropic island (from the Antarctic continent), and this may be driving the Pliocene reduction in ACC strength. Also the Barotropic solver within the model, given a more complex line-integral configuration may not be converging to a solution, this requires further investigation. This change in island specification may also be responsible for the

20   change in ACC geographical extent shown within Table 8. Defining the streamfunction cross section by the latitudes of the centroid and upper 50 % of zonal transport we see that the change in geography (from E^{280}, Eoi^{280}) drives a general latitutudinal thinning of the ACC extent and a shift of its centroid equatorward.

Within the Pliocene experiments, the ACC runs mostly between the surface and sea floor between 60 and 57º S, whilst a deeper countercurrent is present closer to the Peninsula. In the Pacific a pronounced thinning of the ACC latitude extent is

25   observed in which the Sub Antarctic front moves equaterwards (the subtropical front is mostly unchanged). As expected, given the change in geography, the Antarctic Counter Current flows between the Peninsula island and the Antarctic land mass. Within the Pliocene, the model suggests that the Peninsula, now an island, does not impede the flow of the Antarctic Counter current as a component flows poleward of the Peninsula island. There is uncertainty as smaller islands in this region are unrepresented within the model. Figure 14 also suggests a more continuous counter current particularly between 180 and 90º E. The counter

30   current plays an important role in air-sea exchange in the Weddell Sea region, leading to deep convection. This enhanced deep convection within the Pliocene is reflected within Figure 11 and would explain the strengthened AMOC within the Pliocene (Section 4.2.4). This intensified counter current is driven partially by intensified winds poleward of the Sub-Antarctic front (at latitudes > 66 º S) within the Pliocene. The Weddell sub polar gyre is weakened and restructured whilst the Ross Sea Gyre is less intense and extends more equaterward.

Figure 14 also suggests a more continuous counter current particularly between 180 and 90° E. The counter current plays an important role in air-sea exchange in the Weddell Sea region, leading to deep convection. This enhanced deep convection (DC) within the Pliocene is reflected within Figure 11 and could explain the strengthened AMOC within the Pliocene (Section 11), although the limited representation of DC within the model should be noted. This intensified counter current is driven partially

5   by intensified winds poleward of the Sub-Antarctic front (at latitudes > 66 ° S) within the Pliocene. The Weddell sub polar gyre is weakened and restructured whilst the Ross Sea gyre is less intense and extends more equaterward.

4.3 Sensitivity to external boundary conditions

4.3.1 Orbital configuration

Here we examine the sensitivity of the Pliocene climate to choice of orbital configuration (e.g. modern(default) vs. KM5C at

10   3.205 Ma). For Eoi^{400} there is no statistical difference in global means (Tab. 3 MASAT, Tab. 4 MAP, Tab. 6 SST and Warm Pool dynamics). There is a statistical difference in $AMOC_{max}$ between $_{orb}Eoi^{400}$ and Eoi^{400} (t(86)=7.20, p$\ll$.0001) and $AMOC_{max}$ 26.5 N (t(88)=11.36, p$\ll$.0001) using 2-sample t-test assuming unequal variance (null hypothesis being there is a difference in the two timeseries of annual means). With regards to $PMOC_{+ve}$, $_{orb}Eoi^{400}$ and Eoi^{400} are equivalent at the 5% significance level (t(96)=0.62,p=0.54) and similarly, but less significant, for $PMOC_{-ve}$ (t(95)=-1.93, p=0.06). Cyclical variability in the

15   simulated AMOC with a period of 225 years is simulated, so any statistical difference between model simulations for the climatological mean period could simply be due to a lack of coherence between $_{orb}Eoi^{400}$ and Eoi^{400} introduced since the year 2000 fork point.

4.3.2 Total Solar Insolation (TSI)

Section 2.1 identified the possibility of different TSI values being used within PlioMIP2 climate models. Here we determine

20   the sensitivity of HadCM3 within E^{280} and Eoi^{400} experiments to changing the TSI parameter. Reducing total solar insolation from 1365 to 1361 W m^{-2} (- 0.3%) reduces the mean incoming solar (SW) radiation averaged over the entire Earth's surface by 1 W m^{-2} (from 341.25 to 340.25 W m^{-2}). Table 9 accumulates climatological indices from E^{280} and Eoi^{400} under these two TSI values. Figure 15 shows the spatial pattern of climatological differences (Pliocene minus preindustrial) for 1365 to 1361 W m^{-2} for Mean Annual Temperature, Precipitation and Sea Surface Temperature. Overall the patterns of climatological anomalies

25   for the experiments using TSI of either 1361 or 1365W m^{-2} are very similar. In this sense, comparison of model temperature anomalies to proxy temperature anomalies should not generally be influenced by the choice of TSI. However, in a similar way to the chosen orbital configuration, $AMOC_{max}$ does appear sensitive to TSI choice within Eoi^{400} (t(98)=-13.3, p$\ll$.0001) and to a lesser extent E^{280} (t(98)=2.47, p=0.015). It is possible that this AMOC sensitivity to TSI could be a consequence of the previously described coherence within the AMOC cyclicity between Eoi^{400} and $_{1361}Eoi^{400}$.

5 Discussion

In this study we have described the incorporation of PlioMIP2 PRISM4 mid-Piacenzian (Pliocene) enhanced boundary conditions into the HadCM3 global climate model. We conducted PlioMIP2 core and Tier 1 pre-industrial and Pliocene experiments as well as sensitivity experiments exploring solar insolation choice and orbit. We then examined the large-scale features of the
5 climate and ocean state of these experiments.

Comparing to the pre-industrial control (E^{280}), we find Pliocene surface warming focussed within the high-latitudes in a similar distribution to HadCM3 within PlioMIP1 under PRISM3 boundary conditions (Bragg et al., 2012, Exp. 2). We find that the Pliocene palaeogeography and CO_2 account for a warming (relative to the pre-industrial) in globally integrated air temperature (sea surface temperature) of 1.4 ^{o}C (0.8 ^{o}C) and 1.5 ^{o}C (1.0 ^{o}C) respectively. We derive climate sensitivities (for
10 2 x CO_2) of 3.5 ^{o} C and 2.9 ^{o}C for the pre-industrial and Pliocene, which again are similar to PlioMIP of 3.3 ^{o} C and 3.1 ^{o} C respectively (Haywood et al., 2013). We derive an approximation of Earth System Sensitivity of $\sim$5.5 ^{o} C leading to an ESS/CS ratio $\sim$ 1.90, which is similar to the ESS/CS ratio of 2.0 derived within PlioMIP (Haywood et al., 2013). This similarity between PlioMIP1 and PlioMIP2 CS and ESS/CS ratio demonstrates an insensitivity to the degree of palaeogeographic variation between PlioMIP1 and PlioMIP2. This strongly indicates that the primary control on the ESS/CS ratio is the reconstructed
15 ice distribution and global vegetation coverage which, with the exception to the Greenland icesheet, is consistent between PlioMIP1 and PlioMIP2. We recognise that CS and ESS calculations are model dependent and this will be looked at detail in the multi-model comparison of PlioMIP2 results.

We find an AMOC which is more intense in the Pliocene than the pre-industrial driven principally by the change in geography (Table 7). We determine this by comparing AMOC strength between Eoi^{400} and Eoi^{280}. In addition we have explored the
20 sensitivity of AMOC strength to the methodology applied for fresh water correction. The Ei^{280} experiment uses a fixed fresh water correction field corresponding to pre-industrial iceberg trajectories whilst the Pliocene experiment uses an annually-derived correction (Section 2.2), in theory this could impact on simulated AMOC intensity in Eoi^{400} versus Eoi^{280}. To test this we have conducted an additional E^{280} using the annually-derived fresh water correction methodology of Eo^{400} (results not shown). This has demonstrated for the pre-industrial that the fresh water correction method does not lead to a statisti-
25 cally different maximum AMOC strength. This indicates that our intensified AMOC within Eoi^{400} is indeed a consequence of palaeogeographic changes, rather than our approach to fresh water correction. Our intensified Pliocene AMOC is in contrast to Zhang et al. (2013) which found no significant change in the AMOC strength within the PlioMIP1 Exp 2 ensemble. Unfortunately AMOC time-series data is not available from HadCM3 PlioMIP1 (Bragg et al., 2012, Exp. 2) to ascertain the statistical significance of the difference between the PlioMIP1 Pliocene (18.6 Sv) and corresponding pre-industrial (17.8 Sv).
30 Nevertheless, looking at typical HadCM3 (MOSES2) AMOC variability within Table 7, suggests no statistically significant increase in AMOC modelled in PlioMIP1 (the difference between Pliocene and pre-industrial in Bragg et al. being $\sim 1\sigma$). This is the first time using this model that a statistically significant increase in AMOC has been predicted for the Pliocene.

Both the choice of total solar irradiance (TSI; 1361 vs. 1365 W m^{-2}) and the choice of PRISM4 orbital configuration (modern vs. KM5c 3.205 Ma) have been shown not to significantly influence the anomaly-type analysis in use by the Pliocene com-

munity. For example we show that the representation of the KM5c (3.205 Ma) timeslice with a modern orbit is an acceptable choice - leading to no statistically significant differences within MASAT (Table 3) or MAP (Table 4) which is in accordance with previous work (Haywood et al., 2013). When considering absolute values or climatic indices the influence of TSI or orbit is minimal but should nevertheless be considered. Models with greater climate sensitivity will present more sensitivity to TSI

5   and potential for non-linearities in climate response (e.g. relating to feedbacks at or near the sea-ice edge or climate-vegetation interactions).

Whilst the Pliocene represents an incredibly useful contemporary-climate analogue, the use of a non-modern palaeogeography (enhanced PRISM4 boundary condition dataset) does present limitations when using low to intermediate spatial resolution climate models. Numerical regridding of the land sea mask is a binary process and requires hand corrections driven by an un-

10   derstanding of model architecture (i.e. imposed by rigid-lid streamfunction, horizontal grid type etc.) and represented physics. As a pre-cursor, some *a priori* knowledge of important aspects of Pliocene ocean circulation is required to guide a series of expert-informed decisions on model configuration. Similarly, when model development teams (e.g. MOHC) create present-day boundary conditions, knowledge of circulation patterns and through-flow strength is often used to inform hand corrections (e.g artificial deepening of narrow channels) or the inclusion of parametrisations (e.g. diffusive pipes to represent otherwise

15   unrepresented, narrow straits). This *a-priori* knowledge is not necessarily available for the Pliocene and it is therefore difficult to assess. An example of this is in the subariel extension of the UK and its potential influence on the Norwegian Current. An accompanying paper will investigate a number of palaeogeographic sensitivities including regional land-sea mask changes. Additionally, the use of models of varying spatial resolution and model architectures within the PlioMIP2 framework may allow these aspects to be considered. For example, free-surface climate models with higher horizontal spatial resolution may

20   help in the interpretation of the Pliocene ACC strength and the Pliocene Arctic Ocean cold anomaly identified within this study.

Palaeogeographic induced changes in mean state, for example the path of the Antarctic Counter Current around the Peninsula island (Section 4.2.5) represent non-analogous characteristics imposed by the PRISM4 Pliocene reconstruction. Other potentially non-analogous changes are associated with the Maritime continent and subsequent changes in Indonesian through-flow configuration, the closure of the Bering Strait and Canadian Archipelago, and the withdrawal of the Baltic Sea and Hudson

25   Bay. These important regional changes must be considered when considering the mPWP time slice as an equilibrium state analogue to contemporary climate change (i.e. a 400 ppm world).

Data availability.   Climatological averages within NetCDF4 files as specified by the PlioMIP2 experiment specifications held at the University of Leeds data repository. Requests of access should be directed to A. M. Haywood. Specific data requests should be sent to the lead author (S.Hunter@leeds.ac.uk).

30   All PlioMIP2 boundary conditions are available on the USGS PlioMIP2 web page ($http : //geology.er.usgs.gov/egpsc/prism/7\_pliomip2/$).

Author contributions. S. J. H., A. M. H., and A. M. D. designed the study. S. J. H. developed the software framework and conducted the model set-up, spin-up and all data analysis. S. J. H. and J. C. T developed model boundary conditions. S. J. H. wrote the manuscript and incorporated comments from co-authors. Correspondence and requests for materials should be addressed to S. J. H.

Competing interests. The authors declare that they have no conflict of interest.

5 *Acknowledgements.* This work was undertaken on ARC3, part of the High Performance Computing facilities at the University of Leeds, UK. S. J. H., A. M. H., and A. M. D. acknowledge that the work leading up to these results has received funding from the European Research Council under the European Union's Seventh Framework Programme (FP7/2007-2013) ERC grant agreement no. 278636. S. J. H., A. M. H., A. M. D. and J. C. T. acknowledge the Past Earth Network (EPSRC Grant No: EP/M008.363/1). We acknowledge the contribution made by the University of Bristol in keeping the HadCM3 developed and updated

References

Bonham, S. G., Haywood, A. M., Lunt, D. J., Collins, M., and U., S.: El Niño Southern Oscillation, Pliocene climate and equifinality, Philosophical Transactions of the Royal Society A: Mathematical, Physical and Engineering Sciences, 367, 127–156, https://doi.org/10.1098/rsta.2008.0212, 2009.

5 Braconnot, P., Otto-Bliesner, B., Harrison, S., Joussaume, S., Peterchmitt, J.-Y., Abe-Ouchi, A., Crucifix, M., Driesschaert, E., Fichefet, T., Hewitt, C. D., Kageyama, M., Kitoh, A., Laîné, A., Loutre, M.-F., Marti, O., Merkel, U., Ramstein, G., Valdes, P., Weber, S. L., Yu, Y., and Zhao, Y.: Results of PMIP2 coupled simulations of the Mid-Holocene and Last Glacial Maximum Part 1: experiments and large-scale features, Climate of the Past, 3, 261–277, https://doi.org/10.5194/cp-3-261-2007, 2007.

Bragg, F. J., Lunt, D. J., and Haywood, A. M.: Mid-Pliocene climate modelled using the UK Hadley Centre Model: PlioMIP Experiments 1

10 and 2, Geoscientific Model Development, 5, 1109–1125, https://doi.org/10.5194/gmd-5-1109-2012, 2012.

Bryan, K.: Climate and the Ocean Circulation, Monthly Weather Review, 97, 806–827, 1969.

Burls, N. J., Fedorov, A. V., Sigman, D. M., Jaccard, S. L., Tiedemann, R., and Haug, G. H.: Active Pacific meridional overturning circulation (PMOC) during the warm Pliocene, Science Advances, 3, https://doi.org/10.1126/sciadv.1700156, 2017.

Chandler, M. A., Sohl, L. E., Jonas, J. A., Dowsett, H. J., and Kelley, M.: Simulations of the mid-Pliocene Warm Period using two versions

15 of the NASA/GISS ModelE2-R Coupled Model, Geosci. Model Dev., 6, 517–531, https://doi.org/10.5194/gmd-6-517-2013, 2013.

Cox, M. D.: A primitive equation 3-dimensional model of the ocean, Ocean Group Tech. Rep. 1, Tech. rep., 1984.

Cox, P. M., Betts, R. A., Bunton, C. B., Essery, R. L. H., Rowntree, P. R., and Smith, J.: The impact of new land surface physics on the GCM simulation of climate and climate sensitivity, Climate Dynamics, 15, 183–203, https://doi.org/10.1007/s003820050276, https://doi.org/10.1007/s003820050276, 1999.

20 Cunningham, S. A., Alderson, S. G., King, B. A., and Brandon, M. A.: Transport and variability of the Antarctic Circumpolar Current in Drake Passage, Journal of Geophysical Research: Oceans, 108, https://doi.org/10.1029/2001JC001147, 2003.

Cusack, S., Slingo, A., Edwards, J. M., and Wild, M.: The radiative impact of a simple aerosol climatology on the Hadley Centre atmospheric GCM, Quarterly Journal of the Royal Meteorological Society, 124, 2517–2526, https://doi.org/10.1002/qj.49712455117, 1998.

Dolan, A. M., Haywood, A. M., Hill, D. J., Dowsett, H. J., Hunter, S. J., Lunt, D. J., and Pickering, S. J.: Sen-

25 sitivity of Pliocene ice sheets to orbital forcing, Palaeogeography, Palaeoclimatology, Palaeoecology, 309, 98 – 110, https://doi.org/https://doi.org/10.1016/j.palaeo.2011.03.030, special Issue: Climate and seasonality in a Pliocene warm world, 2011.

Dowsett, H., Dolan, A., Rowley, D., Moucha, R., Forte, A. M., Mitrovica, J. X., Pound, M., Salzmann, U., Robinson, M., Chandler, M., Foley, K., and Haywood, A.: The PRISM4 (mid-Piacenzian) paleoenvironmental reconstruction, Climate of the Past, 12, 1519–1538, https://doi.org/10.5194/cp-12-1519-2016, 2016.

30 Dowsett, H. J., Foley, K. M., Stoll, D. K., Chandler, M. A., Sohl, L. E., Bentsen, M., Otto-Bliesner, B. L., Bragg, F. J., Chan, W.-L., Contoux, C., Dolan, A. M., M, H. A., Jonas, J. A., Jost, A., Kamae, Y., Lohmann, G., Lunt, D. J., Nisancioglu, K. H., Abe-Ouchi, A., Ramstein, G., Riesselman, C. R., Robinson, M. M., Rosenbloom, N. A., Salzmann, U., Stepanek, C., Strother, S. L., Ueda, H., Yan, Q., and Zhang, Z.: Sea Surface Temperature of the mid-Piacenzian Ocean: A Data-Model Comparison, Scientific Reports, 3, 2013 EP –, 2013.

Flato, G., Marotzke, J., Abiodun, B., Braconnot, P., Chou, S., Collins, W., Cox, P., Driouech, F., Emori, S., Eyring, V., Forest, C., Gleckler,

35 P., Guilyardi, E., Jakob, C., Kattsov, V., Reason, C., and Rummukainen, M.: Evaluation of Climate Models, book section 9, p. 741?866, Cambridge University Press, Cambridge, United Kingdom and New York, NY, USA, https://doi.org/10.1017/CBO9781107415324.020, 2013.

Gordon, C., Cooper, C., Senior, C. A., Banks, H., Gregory, J. M., Johns, T. C., Mitchell, J. F. B., and Wood, R. A.: The simulation of SST, sea ice extents and ocean heat transports in a version of the Hadley Centre coupled model without flux adjustments, Climate Dynamics, 16, 147–168, https://doi.org/10.1007/s003820050010, 2000.

Griesel, A., Mazloff, M. R., and Gille, S. T.: Mean dynamic topography in the Southern Ocean: Evaluating Antarctic Circumpolar Current transport, Journal of Geophysical Research: Oceans, 117, https://doi.org/10.1029/2011JC007573, 2012.

Haywood, A. M., Dowsett, H. J., Robinson, M. M., Stoll, D. K., Dolan, A. M., Lunt, D. J., Otto-Bliesner, B., and Chandler, M. A.: Pliocene Model Intercomparison Project (PlioMIP): experimental design and boundary conditions (Experiment 2), Geoscientific Model Development, 4, 571–577, https://doi.org/10.5194/gmd-4-571-2011, 2011.

Haywood, A. M., Dolan, A. M., Pickering, S. J., Dowsett, H. J., McClymont, E. L., Prescott, C. L., Salzmann, U., Hill, D. J., Hunter, S. J., Lunt, D. J., Pope, J. O., and Valdes, P. J.: On the identification of a Pliocene time slice for data–model comparison, Philosophical Transactions of the Royal Society A: Mathematical, Physical and Engineering Sciences, 371, 20120 515, https://doi.org/10.1098/rsta.2012.0515, 2013.

Haywood, A. M., Dowsett, H. J., Dolan, A. M., Rowley, D., Abe-Ouchi, A., Otto-Bliesner, B., Chandler, M. A., Hunter, S. J., Lunt, D. J., Pound, M., and Salzmann, U.: The Pliocene Model Intercomparison Project (PlioMIP) Phase 2: scientific objectives and experimental design, Climate of the Past, 12, 663–675, 2016.

Hill, D. J.: The non-analogue nature of Pliocene temperature gradients, Earth and Planetary Science Letters, 425, 232 – 241, https://doi.org/https://doi.org/10.1016/j.epsl.2015.05.044, 2015.

Kopp, G. and Lean, J. L.: A new, lower value of total solar irradiance: Evidence and climate significance, Geophysical Research Letters, 38, https://doi.org/10.1029/2010GL045777, 2011.

Li, D. and Shine, K. P.: A 4-Dimensional Ozone Climatology for UGAMP Models, UGAMP Internal Report No. 35, Tech. rep., 1995.

Lunt, D. J., Valdes, P. J., Haywood, A., and Rutt, I. C.: Closure of the Panama Seaway during the Pliocene: implications for climate and Northern Hemisphere glaciation, Climate Dynamics, 30, 1–18, https://doi.org/10.1007/s00382-007-0265-6, 2008.

Meftah, M., Dewitte, S., Irbah, A., Chevalier, A., Conscience, C., Crommelynck, D., Janssen, E., and Mekaoui, S.: SOVAP/Picard, a Space-borne Radiometer to Measure the Total Solar Irradiance, Solar Physics, 289, 1885–1899, https://doi.org/10.1007/s11207-013-0443-0, 2014.

Meijers, A. J. S., Shuckburgh, E., Bruneau, N., Sallee, J.-B., Bracegirdle, T. J., and Wang, Z.: Representation of the Antarctic Circumpolar Current in the CMIP5 climate models and future changes under warming scenarios, Journal of Geophysical Research: Oceans, 117, https://doi.org/10.1029/2012JC008412, 2012.

Pope, V. D., Gallani, M. L., Rowntree, P. R., and Stratton, R. A.: The impact of new physical parametrizations in the Hadley Centre climate model: HadAM3, Climate Dynamics, 16, 123–146, https://doi.org/10.1007/s003820050009, 2000.

Prescott, C. L., Haywood, A. M., Dolan, A. M., Hunter, S. J., Pope, J. O., and Pickering, S. J.: Assessing orbitally-forced interglacial climate variability during the mid-Pliocene Warm Period, Earth and Planetary Science Letters, 400, 261 – 271, https://doi.org/https://doi.org/10.1016/j.epsl.2014.05.030, 2014.

Roether, W., Roussenov, V. M., and Well, R.: A Tracer Study of the Thermohaline Circulation of the Eastern Mediterranean, pp. 371–394, Springer Netherlands, Dordrecht, https://doi.org/10.1007/978-94-011-0870-6_16, 1994.

Semtner, A. J.: Finite-Difference Formulation of a World Ocean Model, 1974.

Solomon, S., Qin, D., Manning, M., Averyt, K., and Marquis, M.: The Physical Science Basis : Contribution of Working Group I to the
Fourth Assessment Report of the Intergovernmental Panel on Climate Change, vol. 996, Cambridge University Press, https://ci.nii.ac.jp/
naid/10029678161/en/, 2007.

Tindall, J. C. and Haywood, A. M.: Modeling oxygen isotopes in the Pliocene: Large-scale features over the land and ocean, Paleoceanogra-
5   phy, 30, 1183–1201, https://doi.org/10.1002/2014PA002774, 2015.

Valdes, P. J., Armstrong, E., Badger, M. P. S., Bradshaw, C. D., Bragg, F., Crucifix, M., Davies-Barnard, T., Day, J. J., Farnsworth, A.,
Gordon, C., Hopcroft, P. O., Kennedy, A. T., Lord, N. S., Lunt, D. J., Marzocchi, A., Parry, L. M., Pope, V., Roberts, W. H. G., Stone, E. J.,
Tourte, G. J. L., and Williams, J. H. T.: The BRIDGE HadCM3 family of climate models: HadCM3@Bristol v1.0, Geoscientific Model
Development, 10, 3715–3743, https://doi.org/10.5194/gmd-10-3715-2017, 2017.

10   Zhang, Z.-S., Nisancioglu, K. H., Chandler, M. A., Haywood, A. M., Otto-Bliesner, B. L., Ramstein, G., Stepanek, C., Abe-Ouchi, A., Chan,
W.-L., Bragg, F. J., Contoux, C., Dolan, A. M., Hill, D. J., Jost, A., Kamae, Y., Lohmann, G., Lunt, D. J., Rosenbloom, N. A., Sohl,
L. E., and Ueda, H.: Mid-pliocene Atlantic Meridional Overturning Circulation not unlike modern, Climate of the Past, 9, 1495–1504,
https://doi.org/10.5194/cp-9-1495-2013, 2013.
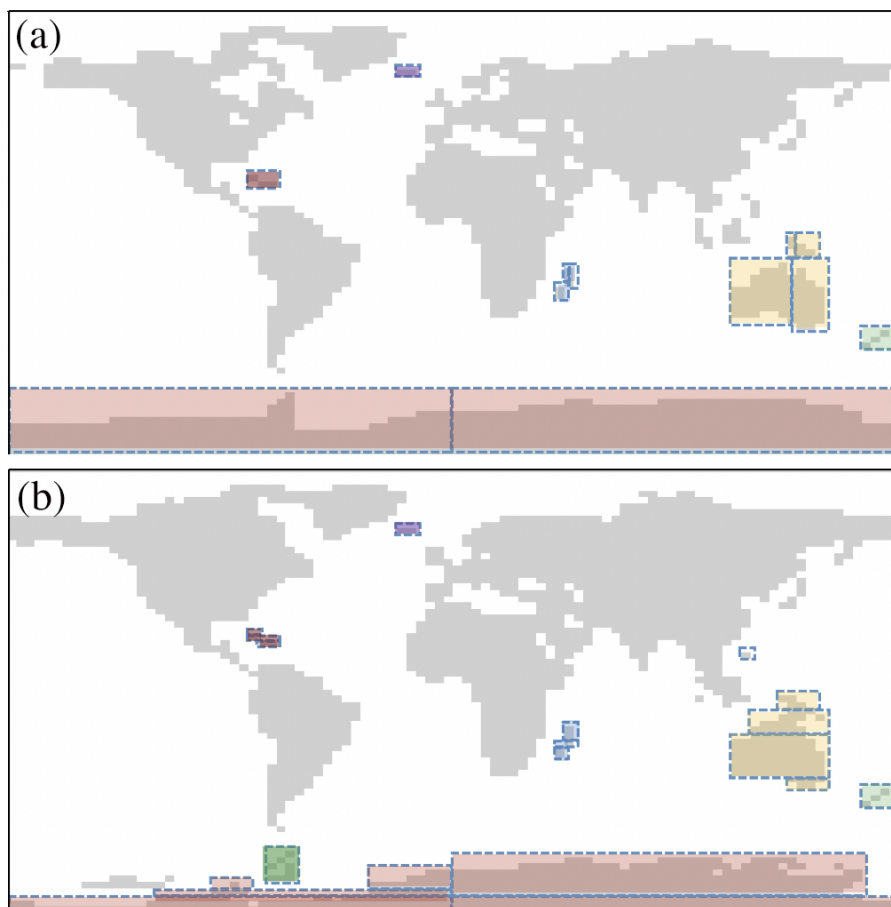
Figure 1. Land Sea Mask and Barotropic island configuration for the (a) pre-industrial and (b) Pliocene.
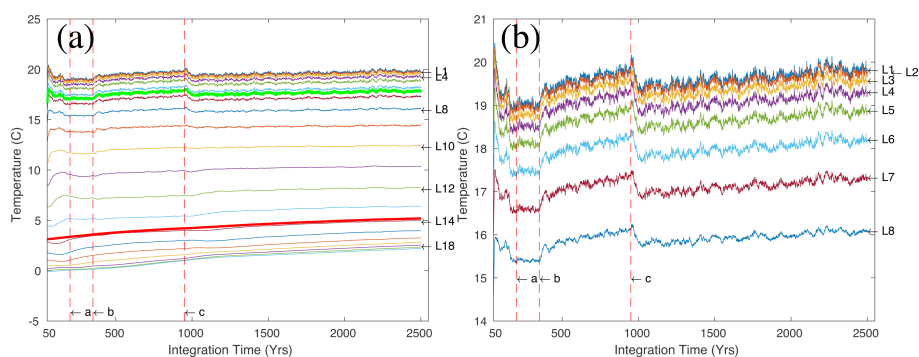
Figure 2. Time-evolution of the globally-integrated temperature for the ocean layers. (a) All ocean levels including whole ocean volume (thick red line), and (b) Ocean layers of the top 200 m. Vertical lines indicate key spin-up stages, [a] Incorporation of barotropic physics into the ocean model, [b] incorporation of barotropic islands into the barotropic solver, and [c] Correction to the barotropic island in the souther high-latitudes and incorporation of full PRISM4 vegetation boundary conditions into the model. Note changes in colour scheme between a) and b).
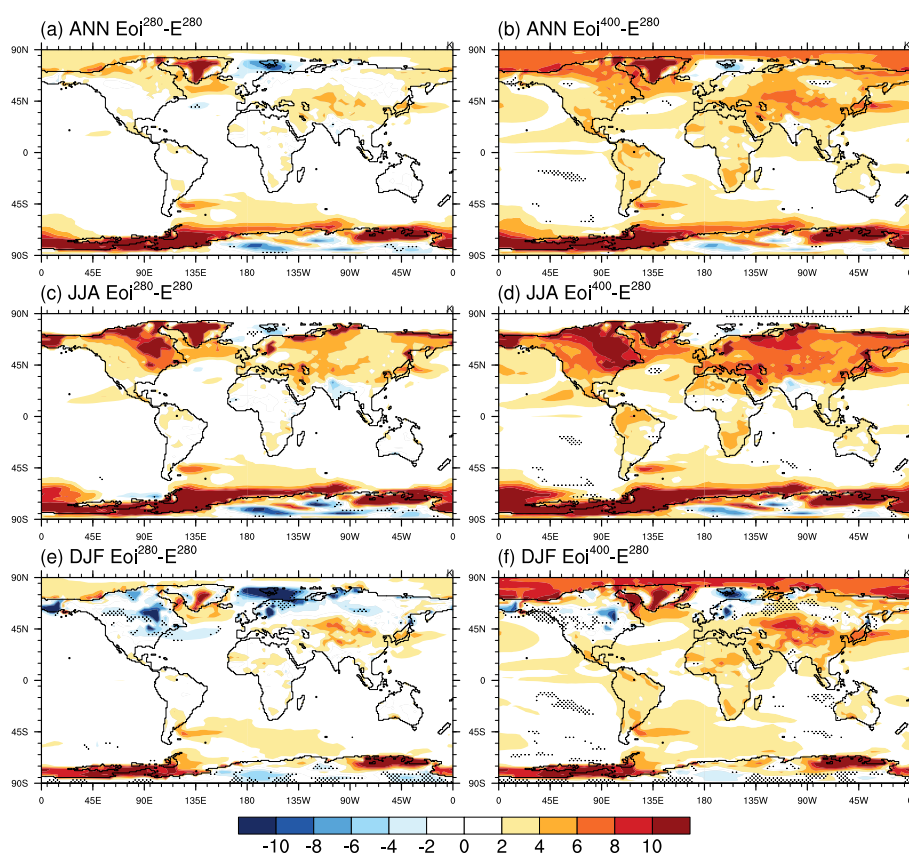
Figure 3. Pliocene (Eoi) MAT anomalies against E^{280}. Stippling indicates regions in which results are not statistically significant at a 95% confidence criteria (independent two-sample student t-test).
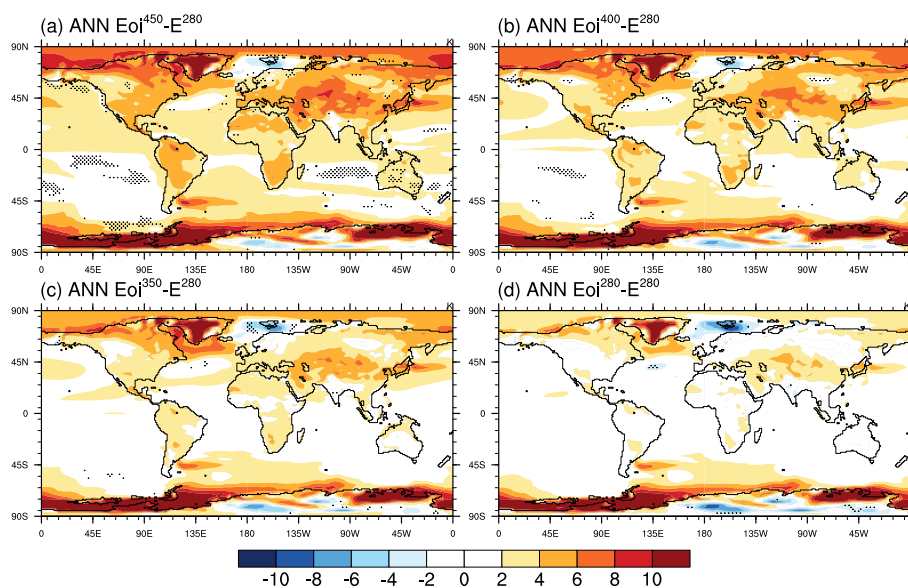
Figure 4. Eoi^{280} and Eoi^{400} Seasonal and MAT anomalies against E^{280}. Stippling indicates regions in which results are not statistically significant at a 95% confidence criteria.
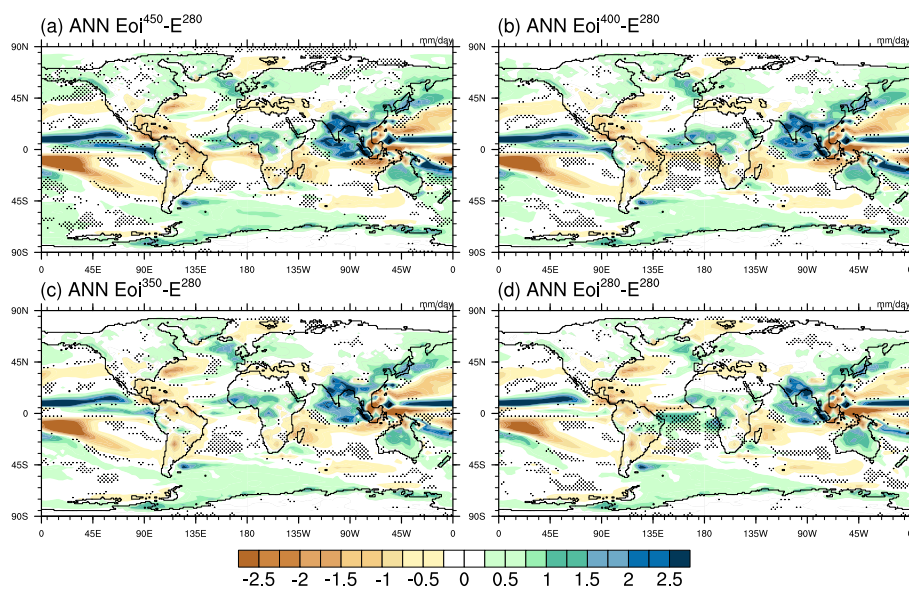
Figure 5. Pliocene Mean Annual Precipitation anomalies (mm day^{-1}) against E^{280}. Stippling indicates regions in which results are not statistically significant at a 95% confidence criteria.
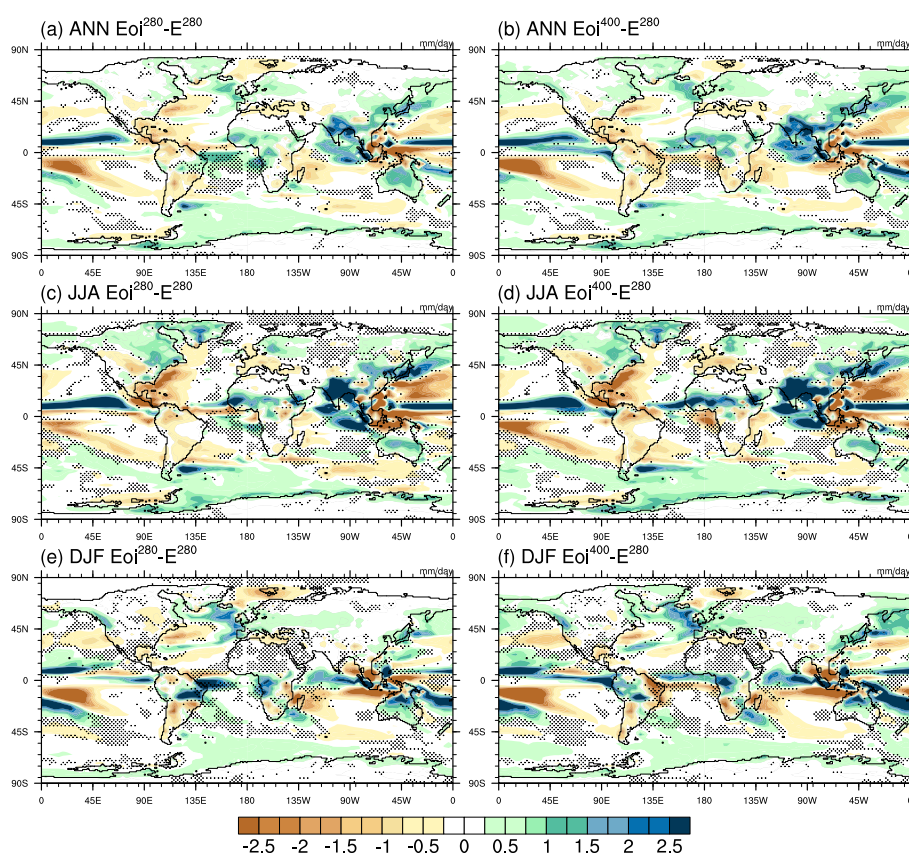
Figure 6. Annual and seasonal Pliocene precipitation anomalies (mm day⁻¹). Stippling indicates regions in which results are not statistically significant at a 95% confidence criteria.
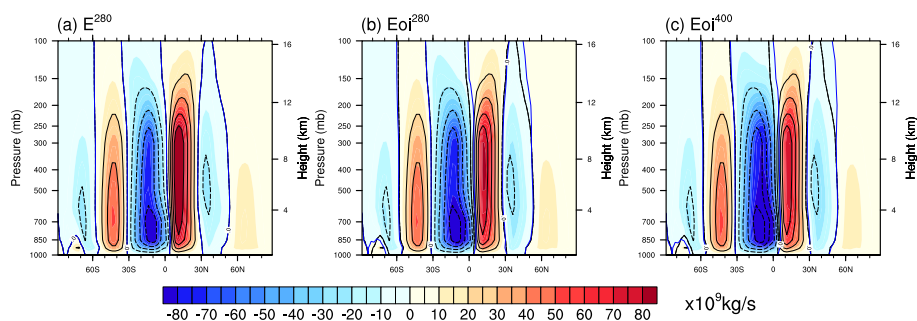
Figure 7. Annual mean zonally-averaged meridional mass stream function for the E ^{280}, Eoi^{280}, and E^{400} experiments. The contour lines are from E^{280} and are every 2x10^{10} kg s^{-1} with dashed lines indicating counterclockwise (looking westward) circulation (ascending air moves southward). The solid blue contour indicates zero meridional streamfunction indicative of the boundary of circulation cells.
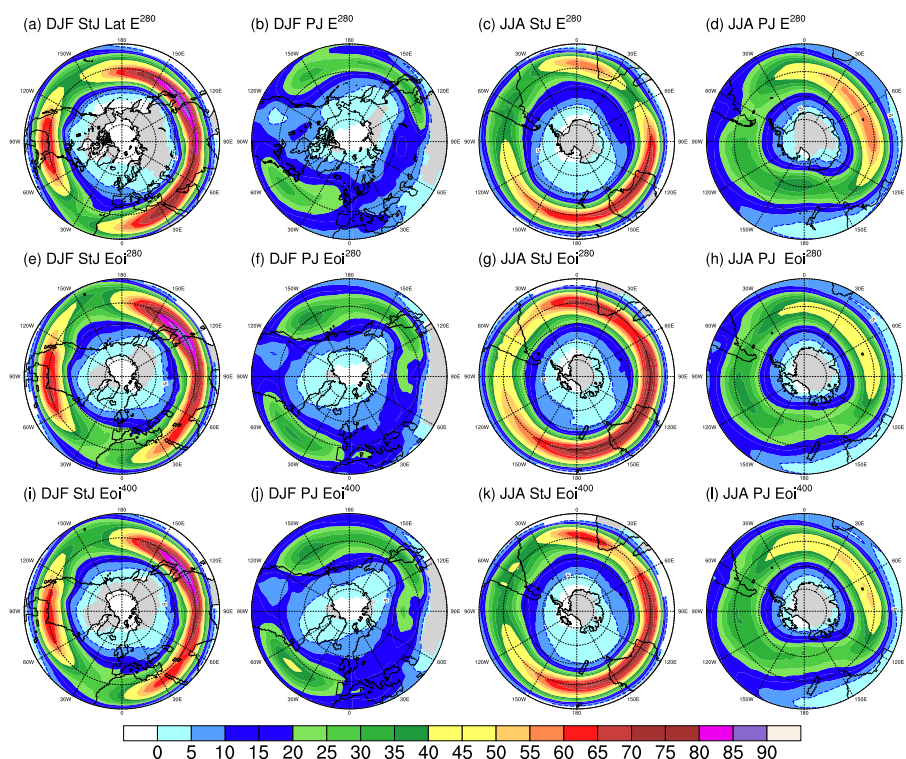
Figure 8. Seasonal (DJF and JJA) distribution of the Subtropical Jet (StJ) and Polar Jet streams (PJ) for E^{280}, Eoi^{280}, and E^{400} experiments. Horizontal speed computed as the mass flux-weighted horizontal speed integrated over 400 - 100 hPa. Colour scale indicates mean number of days within season in which wind speed > 30 ms^{-1}. The Subtropical and Polar jets are differentiated by calculating upper-tropospheric wind shear normalised by the 200 hPa wind speed (following the typology Koch et al., 2006). Note difference in latitude extent between StJ (15 - 90°) and PJ (30 - 90°) plots, the wind-shear classification identifies a jet stream downstream of the Himalayas in our polar jet classification. Note also that this annual-mean state is not physically realised simultaneously, instead represents a histogram of a 50 year climatology.
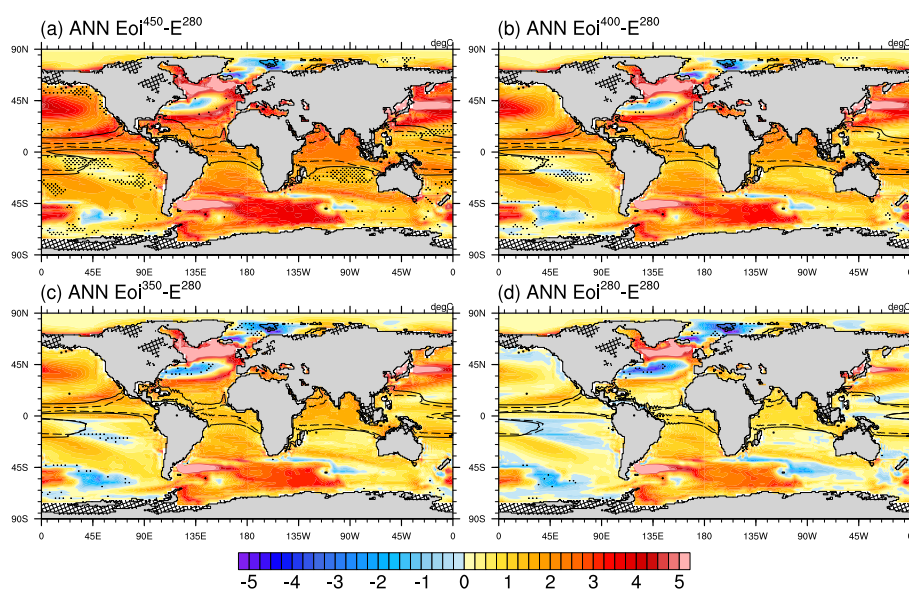
Figure 9. Pliocene (Eoi) SST anomalies against E^{280}. Dotted contour lines indicates E^{280} 28.5° C warm pool whilst the solid contour indicates the Eoi 28° C warm pool. Cross hatching indicates regions in which either modern or pliocene have contrasting land surface. Stippling indicates regions in which there is no statistical difference.
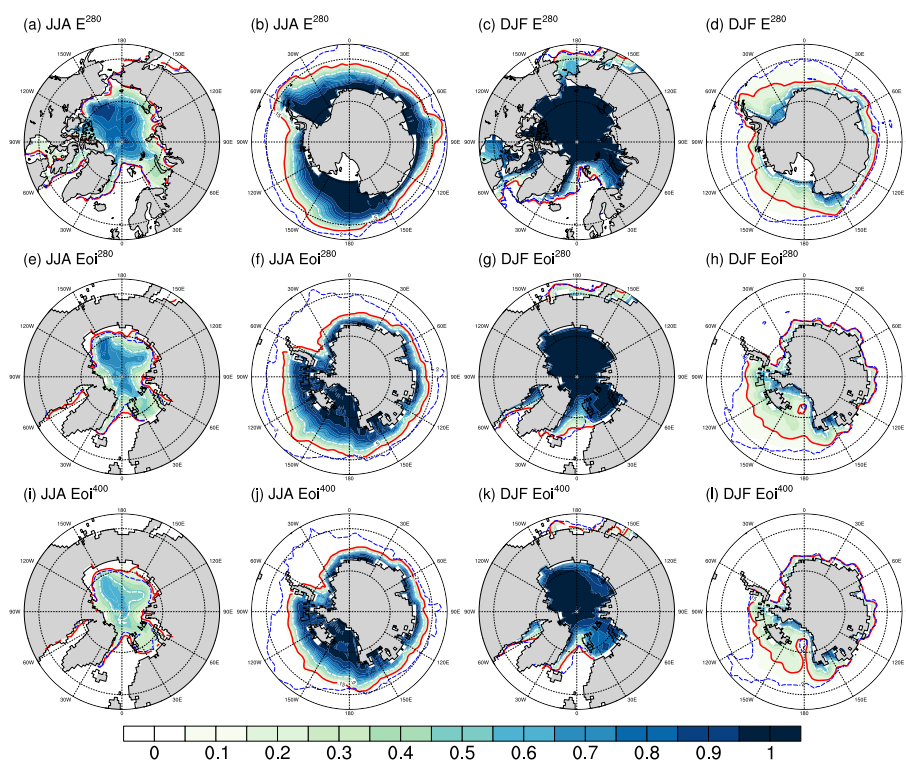
Figure 10. Sea ice concentrations for (a) E^{280}, (b) Eoi^{280}, and (c) Eoi^{400}. The red line indicates the sea ice edge based on a threshold of 15% whilst the dotted white line indicates the 50% threshold. The blue dotted line indicates the 2°C isotherm, in the southern ocean this is indicative of the Antarctic convergence zone (polar front).
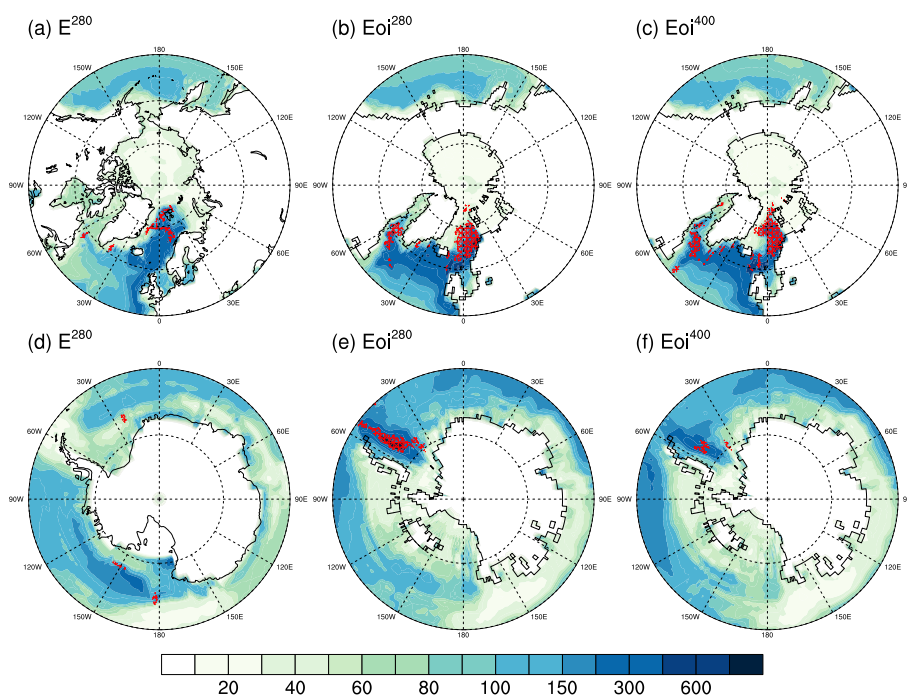
Figure 11. Mean March Northern Hemisphere and September Southern Hemisphere mixed layer depth for (a) E^{280}, (b) Eoi^{280}, and (c) Eoi^{400}. Red hashes indicate regions that exhibit deep (>1000 m) convection at least 1 month during the climatologcal meaning period, single-cell ocean regions have been expanded slightly to improve visualisation.
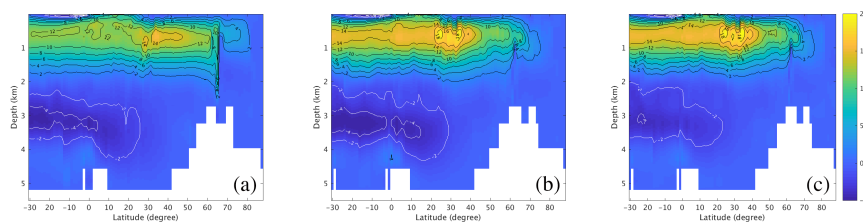
Figure 12. Time-averaged Atlantic Overturning Circulation (AMOC) for (a) E^{280}, (b) Eoi^{280}, and (c) Eoi^{400}.
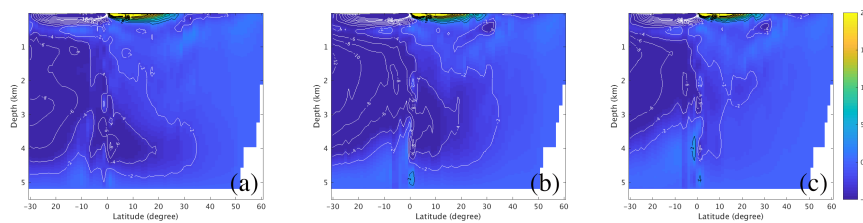
Figure 13. Time-averaged Pacific Overturning Circulation (PMOC) for (a) E^{280}, (b) Eoi^{280}, and (c) Eoi^{400}.
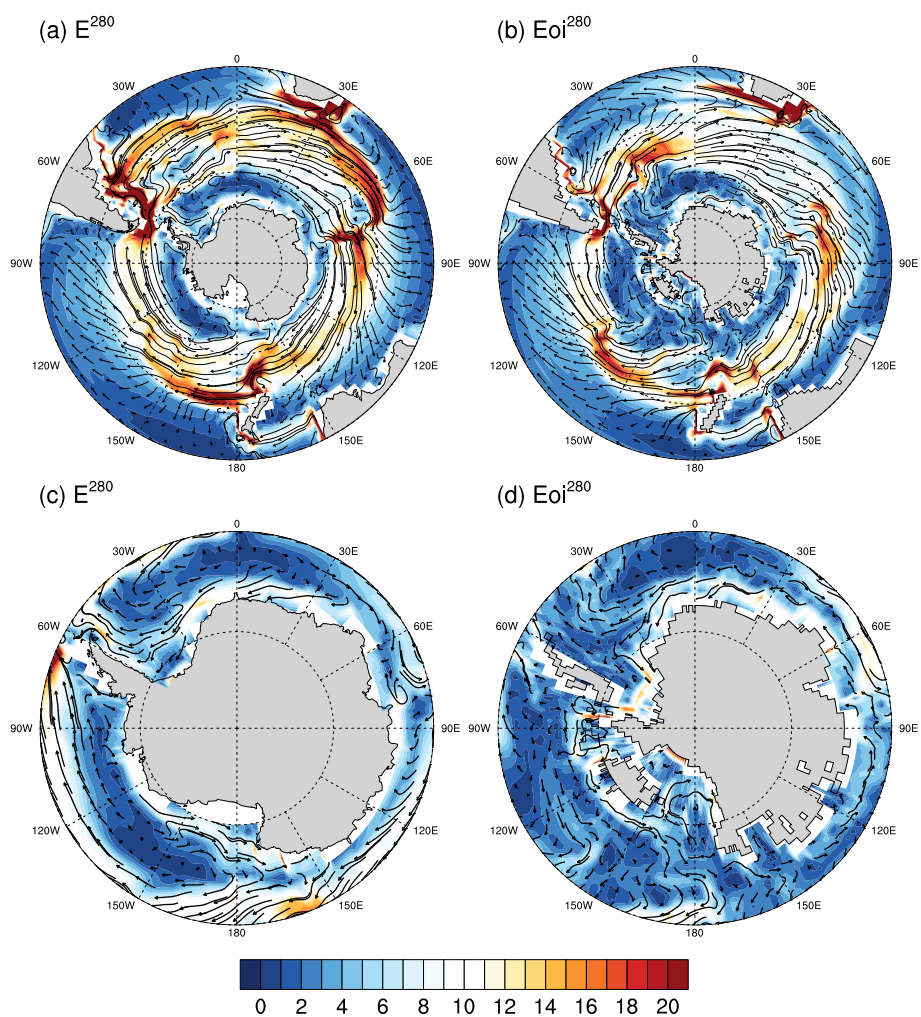
Figure 14. Surface ocean Mean Annual velocity streamlines and vector magnitude E^{280} and Eoi^{280}. Antarctic Counter Current shown within (a) E^{280} and (b) Eoi^{280}, and close-ups showing the counter (coastal) current for the (c) E^{280} and (d) Eoi^{280}.
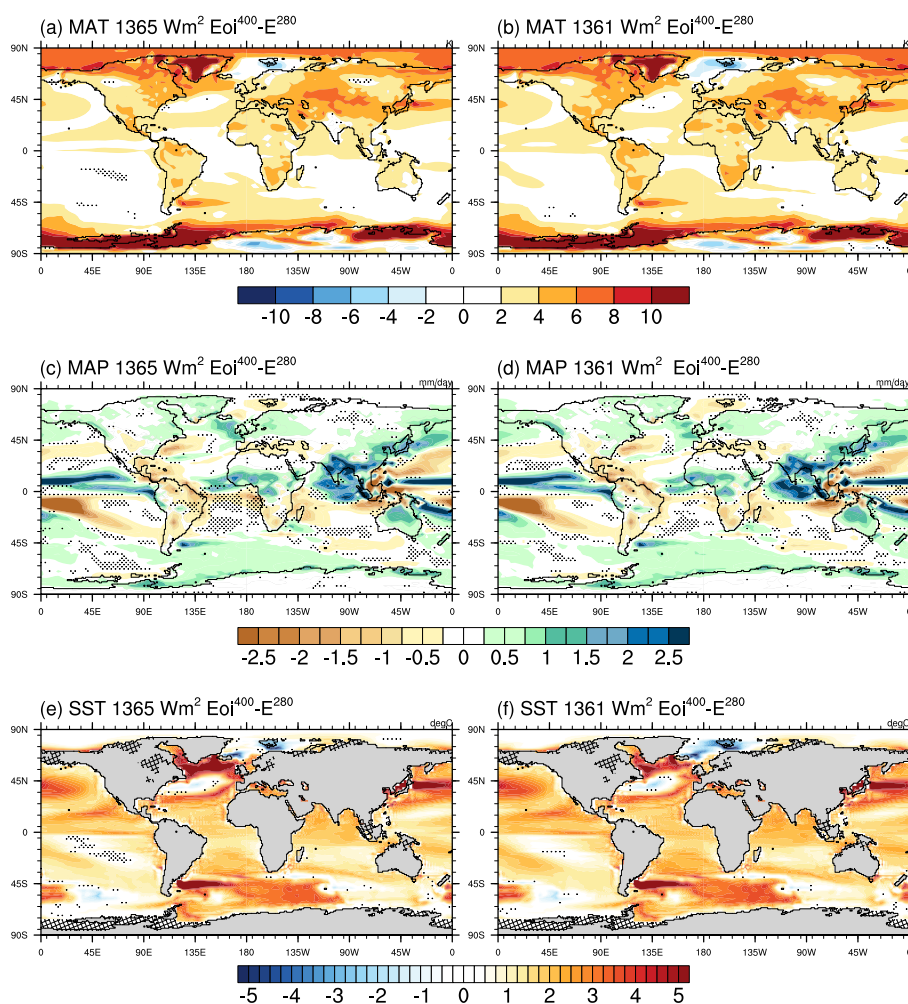
Figure 15. Sensitivity of Eoi^{400} - E^{280} anomalies on TSI values for (a) and (b) Mean Annual Temperature, (c) and (d) Mean annual Precipitation, and (e) and (f) Sea Surface Temperature.

Table 1. Summary of simulations conducted within this study. Those in italic represent simulations beyond the PlioMIP2 experiment design.

ID	PlioMIP2 Status: Tier 1 or 2 (T) & P4F/P4P	Description
Eoi^{400}	CORE	Full enhanced boundary conditions with fixed vegetation and 400 ppm CO_2
Eoi^{450}	T1 P4F & P4P	As Eoi^{400} but with 450 ppm CO_2
Eoi^{350}	T1 P4F & P4P	As Eoi^{400} but with 350 ppm CO_2
Eoi^{280}	T2 P4F & P4P	As Eoi^{400} but with 280 ppm CO_2
E^{280}	CORE	Standard pre-industrial boundary conditions with fixed vegegation and 280 ppm CO_2
E^{400}	T2 P4F & P4P	As E^{280} but with 400 CO_2
E^{560}	T1 P4F	As E^{280} but with 560 CO_2
$_{orb}Eoi^{400}$	Additional sensitivity	As of Eoi^{400} but with 3.205 Myr orbit (KM5c)
$_{orb}Eoi^{450}$	Additional sensitivity	As of Eoi^{450} but with 3.205 Myr orbit (KM5c)
$_{orb}Eoi^{350}$	Additional sensitivity	As of Eoi^{350} but with 3.205 Myr orbit (KM5c)
$_{orb}Eoi^{280}$	Additional sensitivity	As of Eoi^{280} but with 3.205 Myr orbit (KM5c)
$_{1361}Eoi^{400}$	Additional sensitivity	As Eoi^{400} but with TSI=1361 Wm^{-2}
$_{1361}E^{280}$	Additional sensitivity	As E^{280} but with TSI=1361 Wm^{-2}

A description of the additional sensitivities can be found within Section 3. TSI=Total Solar Irradiance, our standard a discussion can be found within Section 2.1 and specific results presented within 4.3.2. KM5c orbital experiments described within 3 and results presented within 4.3.1.

Table 2. Summary of equilibrium state parameters for the seven PlioMIP2 experiments. Globally integrated (Ocean$_{all}$) and surface Ocean (top 200m; Ocean$_{surf}$) Climatological trends and Top of the Atmosphere Energy Balance (TOA$_{EB}$) are derived from the last 100 model years. Note that when underlying trends are small compared to the climatological standard deviation, derivation of the trend is unsatisfactory.

Model	Ocean$_{all}$ (^{o}C cent^{-1})	Ocean$_{surf}$ (^{o}C cent^{-1})	TOA$_{EB}$ (Wm^{-2})
Eoi^{450}	0.063	0.046	0.260
Eoi^{400}	0.041	-0.026	0.047
Eoi^{350}	0.017	0.002	-0.024
Eoi^{280}	0.017	0.002	-0.090
E^{280}	-0.014	0.008	-0.115
E^{400}	-0.048	0.010	0.098
E^{560}	0.107	0.025	0.334

Table 3. Global mean annual surface air temperature (1.5 M; MASAT) decomposed into polar and tropical regions. Polar amplification factor indicated within square brackets, and is defined as the ratio in the anomalies between the pole warming and the global mean warming.

Model	MASAT (° C)	△ T against E[280]	North Pole MASAT (°C)	tropical MASAT (° C)	South Pole MASAT (° C)
Eoi[450]	17.4 ± 0.5	+3.4 ± 0.7	-4.6 ± 1.1 [1.6]	21.6± 0.4	-10.5± 0.9 [2.1]
Eoi[400]	16.9 ± 0.5	+2.9 ± 0.7	-5.2 ± 1.1 [1.7]	21.1 ± 0.4	-11.2 ± 0.8 [2.2]
orbEoi[400]	16.8 ± 0.5	+2.8 ± 0.7	-5.2 ± 1.1 [1.7]	21.1 ± 0.4	-11.4 ± 0.8 [2.2]
Eoi[350]	16.3 ± 0.5	+2.3 ± 0.7	-6.2± 1.0 [1.7]	20.6 ± 0.4	-11.8 ± 0.9 [2.5]
Eoi[280]	15.4 ± 0.5	+1.4 ± 0.7	-8.1 ± 1.1 [1.4]	19.6 ± 0.4	-12.6 ± 0.9 [3.5]
E[280]	14.0 ± 0.5	-	-10.0 ± 1.2	18.7 ± 0.5	-17.5 ± 0.9
E[400]	15.8 ± 0.5	+1.8 ± 0.7	-6.8 ± 1.1	20.3 ± 0.5	-15.5 ± 0.9
E[560]	17.5 ± 0.5	+3.5 ± 0.7	-3.8 ± 1.0	21.9 ± 0.4	-13.4 ± 0.8

Table 4. Global mean Annual mean precipitation (mm day^{-1}).

Model	MAP (mm day^{-1})
Eoi[450]	3.04 ± 0.51
Eoi[400]	3.02 ± 0.51
orbEoi[400]	3.03 ± 0.51
Eoi[350]	3.01 ± 0.51
Eoi[280]	2.98 ± 0.46
E[280]	2.91 ± 0.49
E[400]	2.97 ± 0.53
E[560]	3.02 ± 0.57

Table 5. Integrated mean core latitude of the Subtropical Jet for E[280], Eoi[280] and Eoi[400] experiments during December-January-February (DJF) and June-July-August (JJA) seasons. Note the Subtropical Jet is more stable and persistent than the Polar Jet.

Model	NH DJF	NH JJA	SH DJF	SH JJA
Eoi[400]	32.8 ± 1.5	47.0±2.4	-44.8± 1.9	33.9 ± 1.3
Eoi[280]	32.0 ± 1.1	46.2±1.9	-44.7± 1.8	33.7 ± 1.5
E[280]	30.3 ± 1.4	44.6±3.0	-42.5± 1.3	33.5 ± 1.8

Table 6. Sea surface temperature and defining charactersistics of the equatorial warm pool regions.

Model	MASST (^{o} C)	GWP (x10^6 km^2)	WHWP$_{max}$ (x10^6 km^2)	IPWP$_{max}$ (x10^6 km^2)
Eoi^{450}	20.3 ± 0.4	102.3	25.2 ± 0.6	95.7 ± 2.8 [63.0 ± 2.8]
Eoi^{400}	19.9 ± 0.4	95.7	24.4 ± 0.5	89.0 ± 3.3 [57.1 ± 2.1]
$_{orb}$Eoi^{400}	19.8 ± 0.4	95.3	23.8 ± 0.5	87.4 ± 3.0 [56.2 ± 1.9]
Eoi^{350}	19.6 ± 0.4	88.9	23.1 ± 0.5	82.4 ± 3.7 [50.9 ± 2.6]
Eoi^{280}	18.9 ± 0.4	77.9	19.7 ± 1.2	71.7 ± 3.0 [38.6 ± 3.3]
E^{280}	18.1 ± 0.4	62.6	15.0 ± 1.5	62.8 ± 3.9 [25.4 ± 3.1]
E^{400}	19.3 ± 0.5	89.4	22.1 ± 1.3	85.6 ± 3.9 [50.8 ± 3.2]
E^{560}	20.4 ± 0.4	112.1	27.2 ± 1.5	102.9 ± 2.5 [68.9 ± 2.6]

The Global Warm Pool (GWP) area defined using Mean Annual Sea Surface Temperature (MASST) and a 28 ^{o} C.
Western Hemisphere Warm Pool (WHWP; 130° W - 45° W), Indo - Pacific Warm Pool (IPWP; 30° E - 60° W) are
defined as the max monthly mean area that is 28° C. For IPWP$_{max}$ the number in parenthesis is the area that is 28°
C year-round.

Table 7. Atlantic and Pacific Meridional Overturning Circulation

Model	AMOC$_{max}$ (Sv)	AMOC$_{max}$ 26.5 N (Sv)	PMOC$_{+ve}$ (Sv)	PMOC$_{-ve}$ PDW ≥30 S >500 m (Sv)
Eoi^{450}	18.6 ± 1.1	16.3 ± 1.0	39.3 ± 4.0	-9.3 ± 1.5 [1000 m]
Eoi^{400}	19.6 ± 1.0	17.2 ± 0.8	40.6 ± 3.0	-9.1 ± 1.4 [1000 m]
$_{orb}$Eoi^{400}	21.4 ± 1.5	19.3 ± 1.1	40.9 ± 3.3	-9.8 ± 1.9 [1000 m]
Eoi^{350}	20.4 ± 1.1	18.8 ± 0.9	42.2 ± 3.9	-9.8 ± 1.8 [1000 m]
Eoi^{280}	18.9 ± 0.8	17.4 ± 0.9	46.0 ± 3.4	-12.3 ± 1.6 [1500 m]
E^{280}	15.7 ± 1.2	13.4 ± 1.1	33.4 ± 3.1	-8.6 ± 1.4 [2700 m]
E^{400}	15.2 ± 1.2	13.6 ± 1.0	29.3 ± 2.5	-9.0 ± 0.9 [3960 m]
E^{560}	15.9 ± 1.3	13.8 ± 0.9	25.0 ± 2.1	-7.6 ± 0.8 [3960 m]

The maximum of the Atlantic Meridional Overturning Circulation (AMOC) is referred to as the meriodonal overturning
index (MOI) after Delworth et al., 1993. Pacific Meridional Overturning Circulation (PMOC).

Table 8. Characteristics of the Antarctic Circumglobal Current for the Pliocene and pre-industrial experiments. From the Barotropic stream-function we derive the Mean ACC latitude (the Polar front) from the centroid of the zonal transport and the core width derived from the $\pm$ 50% boundary.

Model	ACC at 65º W (Sv)	Mean ACC latitude (ºS)	Mean ACC core width (º)
Eoi^{450}	78.3 $\pm$ 2.9	58.8	11.5
Eoi^{400}	76.7 $\pm$ 2.8	58.8	11.8
$_{orb}$Eoi^{400}	77.3 $\pm$ 2.9	58.7	11.8
Eoi^{350}	73.5 $\pm$ 3.0	58.8	11.9
Eoi^{280}	51.6 $\pm$ 31.9	60.0	12.6
E^{280}	179.0 $\pm$ 11.2	66.0	33.6
E^{400}	186.6 $\pm$ 9.0	66.6	33.3

Table 9. Sensitivity of E^{280} and Eoi^{400} (and their corresponding anomalies) to TSI of 1361 and 1365 W m^{-2}. Mean Annual Surface Air Temperature (MASAT), Mean Annual Precipitation (MAP), Mean Annual Sea Surface Temperature (MASST), Atlantic and Pacific Meridional Circulation (AMOC$_{max}$ and PMOC$_{+ve,-ve}$) derivation as of Section 4.2.4, and Antarctic Circumpolar Current (ACC) derivation as of Section 4.2.5.

Model	MASAT	MAP	MASST (º C)	AMOC$_{max}$	PMOC$_{+ve,-ve}$	ACC
E^{280}	14.0 $\pm$ 0.5	2.91 $\pm$ 0.49	18.1 $\pm$ 0.4	15.7 $\pm$ 1.2	33.4 $\pm$ 3.1, -8.6 $\pm$ 1.4	179.0 $\pm$ 11.1
$_{1361}$E^{280}	13.7 $\pm$ 0.5	2.89 $\pm$ 0.48	17.9 $\pm$ 0.4	16.3 $\pm$ 1.2	33.8 $\pm$ 3.9, -9.2 $\pm$ 1.5	180.0 $\pm$ 6.2
Eoi^{400}	16.9 $\pm$ 0.5	3.02 $\pm$ 0.51	19.9 $\pm$ 0.4	19.6 $\pm$ 1.0	40.6 $\pm$ 3.0, -9.1 $\pm$ 1.4	76.7 $\pm$ 2.8
$_{1361}$Eoi^{400}	16.7 $\pm$ 0.5	3.01 $\pm$ 0.50	19.7 $\pm$ 0.4	17.0 $\pm$ 0.9	37.7 $\pm$ 3.3, -8.5 $\pm$ 1.7	76.0 $\pm$ 2.5
Eoi^{400}-E^{280}	2.9 $\pm$ 0.7	0.11 $\pm$ 0.71	1.8 $\pm$ 0.6	3.9 $\pm$ 1.6	7.2 $\pm$ 4.3, -0.5 $\pm$ 2.0	-102.3 $\pm$ 11.4
$_{1361}$Eoi^{400}-$_{1361}$E^{280}	3.0 $\pm$ 0.7	0.12 $\pm$ 0.69	1.8 $\pm$ 0.6	0.7 $\pm$ 1.5	3.9 $\pm$ 5.1, 0.7 $\pm$ 1.3	-104.0 $\pm$ 6.7